

Experimental and numerical studies on moderate-(Formula presented) aerodynamics of cambered thick wingsails in crescent shape

Downloaded from: https://research.chalmers.se, 2026-11-08 12:54 UTC

Citation for the original published paper (version of record):
Zhu, H., Chernoray, V., Ringsberg, J. et al (2026). Experimental and numerical studies on moderate-(Formula presented) aerodynamics of cambered thick wingsails in crescent shape. Journal of Ocean Engineering and Science, 11(6): 2345-2361. http://dx.doi.org/10.1016/j.joes.2026.08.012

N.B. When citing this work, cite the original published paper.

research.chalmers.se offers the possibility of retrieving research publications produced at Chalmers University of Technology. It covers all kind of research output: articles, dissertations, conference papers, reports etc. since 2004. research.chalmers.se is administrated and maintained by Chalmers Library

(article starts on next page)

Journal of Ocean Engineering and Science 11 (2026) 2345–2361

Contents lists available at ScienceDirect

Journal of Ocean Engineering and Science

journal homepage: www.elsevier.com/locate/joes

Research Paper

Experimental and numerical studies on moderate-*Re* aerodynamics of cambered thick wingsails in crescent shape

Heng Zhu (朱恒)[a,*], Valery Chernoray [b], Jonas W. Ringsberg [a], Bengt Ramne [c], Hua-Dong Yao (姚华栋)[a]

[a] Chalmers University of Technology, Department of Mechanical Engineering, Division of Marine Technology, Gothenburg, Sweden
[b] Chalmers University of Technology, Department of Mechanical Engineering, Division of Fluid Dynamics, Gothenburg, Sweden
[c] ScandiNAOS AB, Gothenburg, Sweden

ARTICLE INFO

Keywords:
Crescent-shaped thick wingsail
IDDES
Moderate Reynolds number
Multi-wingsail interference
Wind-assisted ship propulsion
Wind tunnel test

ABSTRACT

For wind-assisted ship propulsion (WASP), wingsails with cambered sectional profiles like crescent-shaped ones have shown great potential considering high thrust generation. However, there have been few experimental and numerical studies to address such wingsails at moderate Reynolds numbers (*Re*), of which knowledge is important for guiding fast design. In this study, the aerodynamics of a crescent-shaped wingsail at a range of moderate *Re* is investigated in isolated and triple-sail situations. Wind tunnel tests and high-fidelity computational fluid dynamics (CFD) simulations, which use the improved delayed detached eddy simulation (IDDES) approach, are conducted. The wingsails of two aspect ratios (5.3 and 3.6 corresponding to semi-retracted and fully expanded sails in practice) are analyzed at the angles of attack from 0° to 90°, and *Re* from 1.8×10^5 to 3.6×10^5. In addition to general aerodynamic characteristics, a specific crisis of the aerodynamic forces is found at the angle of attack of 15° when *Re* is reduced to 2.7×10^5, which does not exist in conventional NACA-profile wingsails. When triple wingsails are arranged in a row, the velocity fields between the sails interact, although the vortex patterns in their wakes remain similar. This interference leads to significant redistribution of the aerodynamic forces between the wingsails in the arrangement. The total thrust from the triple wingsail arrangement under the side-wind condition is close to three times the thrust of a single wingsail.

1. Introduction

Currently, more than 80% of global freight transport by volume is carried out via shipping, which is a major contributor to greenhouse gas (GHG) emissions [1]. To address this, the International Maritime Organization (IMO) has set an ambitious target to cut GHG emissions from the shipping industry by 50% compared to 2008 levels by 2050 [2]. Among the strategies to achieve this goal, wind-assisted ship propulsion (WASP) for cargo ships has emerged as a highly promising solution to reduce reliance on fossil fuels. Several innovative WASP technologies, such as wingsails, Flettner rotors, and kite sails, have been developed in recent decades [3,4]. Among these concepts, wingsails have some advantages [5]. For instance, wingsails perform better than kite sails and Flettner rotors under sidewind and downwind conditions, respectively.

Winds can be from both the starboard and the port side of a ship during operation, so early wingsails were designed with symmetrical section profiles [6]. However, recently, more designs of wingsails have incorporated a cambered sectional profile, as shown in Fig. 1, to increase the lift force which contributes to the thrust force (F_T) under side-wind conditions.

It should also be mentioned that two- and three-element profiles are also popular concepts nowadays [13]. These concepts are combinations of a main foil with one or two flaps [14]. By rotating the flaps, a camber can also be made by these concepts [15]. Conventional airfoil profiles, *e.g.*, NACA 0015, are normally used, so that the characteristics of the flow field induced by these wingsails do not show significant differences from other similar applications like airplane wings [13,16,17]. However, compared with these multi-element wingsails, from the practical perspective, the wingsails in Fig. 1 have simpler geometries that are easier to manufacture and operate under downwind conditions due to the symmetric edges [5].

To obtain an accurate estimation of the propulsive performance of

* Corresponding author.
E-mail address: heng.zhu@chalmers.se (H. Zhu).

https://doi.org/10.1016/j.joes.2026.08.012
Received 4 October 2024; Received in revised form 6 April 2026; Accepted 30 August 2026
Available online 31 August 2026
2468-0133/© 2026 THE AUTHORS. Published by Elsevier B.V. on behalf of Shanghai Jiao Tong University. This is an open access article under the CC BY license (http://creativecommons.org/licenses/by/4.0/).

cambered wingsails, high-fidelity simulations using computational fluid dynamics (CFD) have been conducted [10–12,18–23]. According to these studies, compared to symmetric airfoil profiles, the cambered wingsails provide higher lift force coefficients (C_L) at small angles of attack (α) and higher drag force coefficients (C_D) at large α, leading to a better propulsive performance. On the other hand, it was found that due to the large camber of the sectional profile, significant flow separation is induced, which increases the unsteadiness of the flow field and aerodynamic loads.

Aside from CFD simulations, wind tunnel (WT) tests have been conducted for wingsails [24–27]. Nevertheless, the tested wingsails have conventional airfoil profiles without camber. Since the aerodynamic characteristics of cambered profiles are quite different from zero-cambered NACA ones [23], the previous experimental findings cannot be directly applied to the evaluation of the cambered foils, for example, flow separation and reattachment, and vortex shedding.

In addition to wingsail studies, it is also necessary to review the experimental work on sailing yacht sails, since they represent another important class that provide useful reference for understanding flow behavior of cambered configurations. Experimental studies have been carried out for sails of sailing yachts [28–32], while it is worth noting that such sails have much lower Reynolds numbers (*Re*). The sectional profiles of yacht sails are usually regarded as a cambered arc with sharp edges [30,33]. *Re* that can be achieved in the WT normally has the order of magnitude of 10^4 to 10^5, which is similar to that for a full-size yacht sail. For wingsails used for large commercial ships, the order of magnitude of *Re* is normally 10^7 [34,35]. Yacht sails are simply shaped in thin plates, whereas wingsails are cambered and shaped in thicker airfoils. This raises a question about whether the knowledge of yacht sails is also valid for the cambered thick wingsails.

Based on the literature survey above, crescent-shaped wingsails with thick sectional profiles have not been studied through experiments. Besides, the aerodynamics at moderate *Re* have not been addressed for both isolated and multi-sail situations, although the knowledge is useful for developing fast simulation methods in the early design stage. To fill this knowledge gap, the present study is primarily based on a systematic set of WT tests to understand the aerodynamic characteristics, especially the force coefficients at different α and their sensitivity to *Re*. In addition, for a triple-wingsail arrangement, various yaw angles (β), *i.e.*, apparent wind angles (θ_{AW}) are considered. Complementary CFD simulations are further conducted for the single- and triple-wingsail arrangement to visualize the flow fields, offer additional physical insights, and support the interpretation of the experimental results.

2. Methods

2.1. Concept design

2.1.1. Wingsail arrangement

For ships equipped with rigid wingsails, the wind loads on the sails contribute to the overall thrust that propels the ship forward. Fig. 2 illustrates the wind triangle [36], where V_S represents the ship's speed, V_{TW} represents the true wind speed, and θ_{TW} represents the true wind angle. The apparent wind speed (V_{AW}), which is the wind speed perceived relative to the ship, and the apparent wind angle (θ_{AW}) can be determined using Eqs. (1) and (2), respectively. It should be noted that the principle of sailing in Fig. 2 is based on two-dimensional assumption

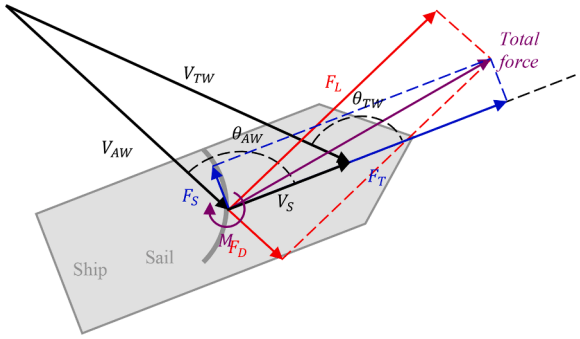


Fig. 2. The wind triangle and loads on the sails [36,5].

and the leeway [37] is neglected, so ship speed vector is aligned with the centerline of the ship.

$$V_{AW} = \sqrt{V_S^2 + V_{TW}^2 + 2V_S V_{TW}\cdot\cos\theta_{TW}} \tag{1}$$

$$\theta_{AW} = \tan^{-1}\left(\frac{V_{TW}\cdot\sin\theta_{TW}}{V_S + V_{TW}\cdot\cos\theta_{TW}}\right) \tag{2}$$

As shown in Fig. 2, the force component parallel to the ship velocity is the thrust denoted as F_T, and the perpendicular one is the side force as F_S. These force components can be calculated based on the lift and drag forces, F_L and F_D, using Eqs. (3) and (4) [36]. The side force does not account for the propulsion but causes heeling, rolling, drifting, and additional induced resistance.

$$F_T = F_L\cdot\sin\theta_{AW} - F_D\cdot\cos\theta_{AW} \tag{3}$$

$$F_S = F_L\cdot\cos\theta_{AW} + F_D\cdot\sin\theta_{AW} \tag{4}$$

C_L can be calculated by Eq. (5), where ρ_{air} is the density of the air, and A_S is the reference area of the wingsail.

$$C_L = \frac{F_L}{\frac{1}{2}\rho_{air}V_{AW}^2 A_S} \tag{5}$$

Similarly, C_D and the thrust force coefficient (C_T) can be defined. To separate full-scale ship and the WT tests, different nomenclatures are used in this study. V_∞ is the inlet wind speed in the WT tests, corresponding to V_{AW} for a ship. β is the yaw angle in the WT tests, which corresponds to θ_{AW} for a ship.

To capture as much wind power as possible, more than one wingsail can be installed on ships [38]. This study explores a triple-wingsail layout where three wingsails are installed along the centerline of the ship, as shown in Fig. 3. According to Zhu, Yao, et al. [12], the maximum C_L is achieved at the angle of attack of $\alpha = 20^\circ$. Therefore, this angle of attack is chosen in this study. A series of operation conditions with different β (from 80° to 120°) are investigated. The distance between the masts of the wingsails, which corresponds to the distance between their rotational axes in the WT, is 1.5 times the chord length (L_c). For the convenience of discussing the triple-wingsail system, the three sails are termed in Fig. 3. For instance, the sail closest to the bow of the ship is called "Sail 1".

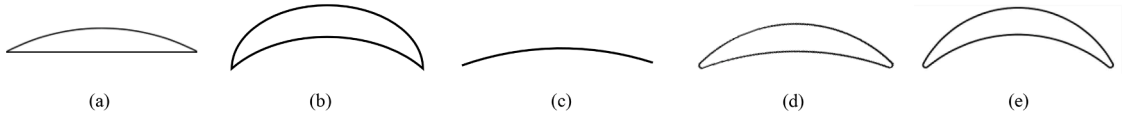


Fig. 1. Schematics of cambered wingsail profiles: (a) segment-shaped [7]; (b) crescent-shaped [8]; (c) arc-shaped [9]; (d) crescent-shaped [10,11]; (e) crescent-shaped [12].

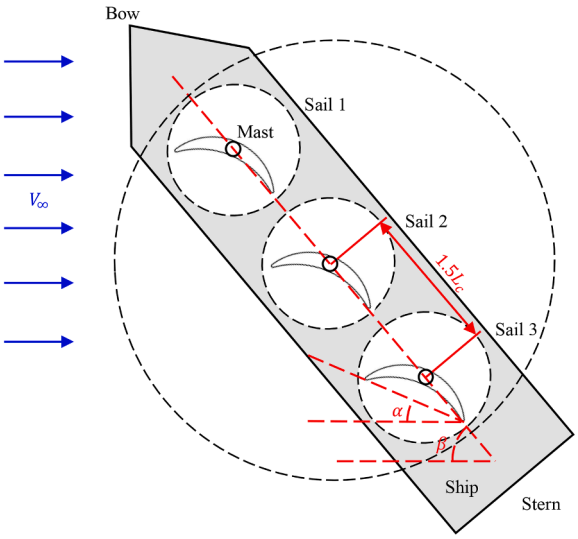


Fig. 3. Triple-wingsail layout.

2.1.2. Crescent-shaped wingsail

A crescent-shaped wingsail has been developed and documented in previous studies [5,10–12]. Previous studies have shown that crescent-shaped profiles exhibit a higher thrust force coefficient and are easier to handle when the wind direction shifts from starboard to port under downwind conditions [5,11,23]. Additionally, the large camber of these profiles leads to higher C_D at $\alpha \sim 90°$, which enhances propulsive performance in downwind scenarios [11,39,40].

The crescent-shaped profile is a simple design formed by a combination of circles and arcs [41], as illustrated in Fig. 4. This profile shape is determined by four parameters: L_c, the diameter of the mast corresponding to the profile thickness at half-chord, the radius of the edges, and the radius of the suction-side arc. Based on parametric sensitivity analyses conducted through two-dimensional CFD simulations [10,12], an optimal profile, termed "D2R8," has been identified. In this profile, the four parameters in full scale are 14 m, 2 m, 0.2 m, and 8 m, respectively. The shape of the sectional profile remains the same through the spanwise direction. The wingsail height (H) is adjustable in practice, so two aspect ratios, 5.3 (with $H = 0.74$ m) and 3.6 (with $H = 0.50$ m) are tested.

2.1.3. Coordinate systems

The Cartesian coordinate systems are introduced by following Zhu, Yao, et al. [12], as shown in Fig. 5. The X-axis is aligned with the streamwise direction. The origin is located at the center of the bottom surface in the isolated single-wingsail case. For the triple-wingsail case, the origin is at the center of the bottom surface of "Sail 2," as shown in Fig. 5(b).

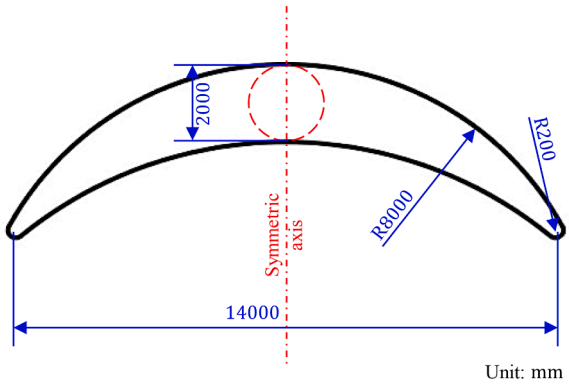
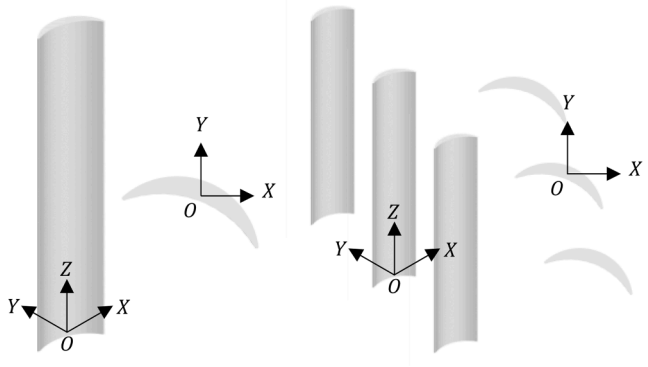


Fig. 4. Crescent-shaped profile (dimensions for full-scale) [12].



(a) Single wingsail. (b) Triple wingsails.

Fig. 5. The coordinate systems of the isolated and triple-sail cases.

2.2. WT test

2.2.1. WT facilities

The WT tests are carried out in the Laboratory of Fluids and Thermal Science within the Department of Mechanics and Maritime Sciences at Chalmers University of Technology. A schematic of the Chalmers WT is presented in Fig. 6(a). This WT features a closed test section. Air is circulated through the closed circuit by a motor and fan located in the return channel. A honeycomb structure and three screens are positioned upstream of the test section to ensure uniform airflow in terms of speed and direction. An air gap at the rear of the test section helps regulate the pressure within the WT. The test section, where the wingsails are installed and tested, has an octagonal cross-section, as illustrated in Fig. 6(b).

The maximum inflow speed V_∞ (*i.e.*, the apparent wind speed V_{AW} in practice) of this study is 40 m/s, leading to a Mach number (Ma) of 0.12. Since the Mach number is smaller than 0.3, the flow is regarded as incompressible. The inlet turbulence level is $< 0.5\%$ under the testing conditions of the present study. The environmental conditions, such as the absolute pressure and temperature are monitored and logged during the test. The measurements show insignificant variations, so both values are assumed to be constant in the analysis. The temperature is considered $23°C$, and the ambient static pressure is 101.3 kPa, so the density of air (ρ_{air}) is 1.18 kg/m^3, and the kinematic viscosity (υ) is 1.56×10^{-5} m^2/s.

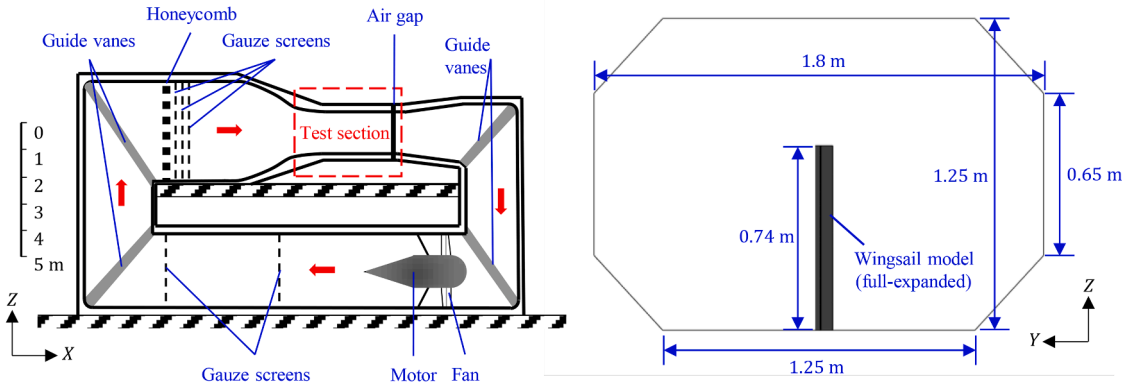
2.2.2. Scale models

Fig. 7 illustrates the schematic setup for the installation and measurement process in the WT tests. The test models are constructed from aluminum. The deck supporting the test models is designed to be able to rotate, allowing for adjustments of the angles of attack (α) and yaw (β), as depicted in Fig. 3. A set of gearboxes [11] is installed beneath the deck panel to control the rotation.

To trigger the transition from laminar to turbulent flow on the wingsail suction side, a tripping tape [11,42,43] is attached to the wingsail suction side surface at $0.1L_c$ near the leading edge [11]. A figure in Supplementary materials shows the configuration of the tripping tape. The tape has a thickness of 0.5 mm and a width of 5 mm.

2.2.3. Measurements

2.2.3.1. Force measurement. To measure lift and drag forces, an external balance placed under the test section floor is adapted to hold the deck with the wingsail models. A compact 6-component balance is used under the middle wing sail. The balances are controlled and monitored by LabVIEW software, displaying measured data in real time.



(a) Two-dimensional schematic of the WT in the laboratory of Fluids and Thermal Science at Chalmers University of Technology.

(b) Dimensions of the cross-section of the WT test section.

Fig. 6. Schematic of the Chalmers WT.

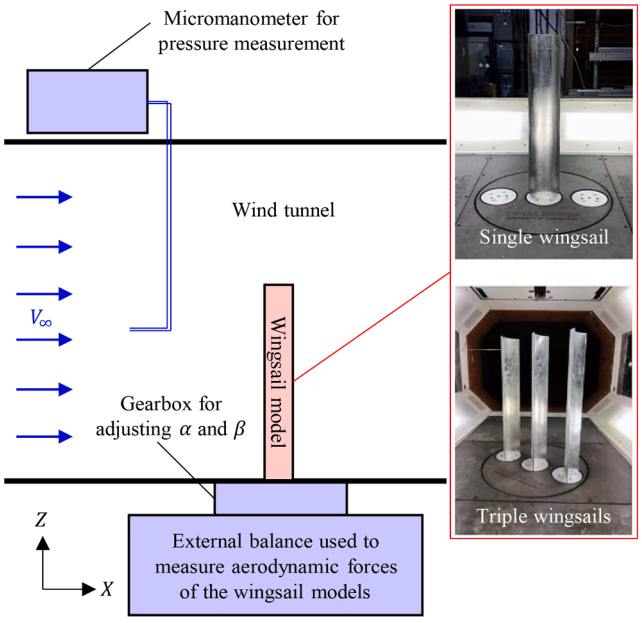


Fig. 7. Schematic of WT test installation and measurements.

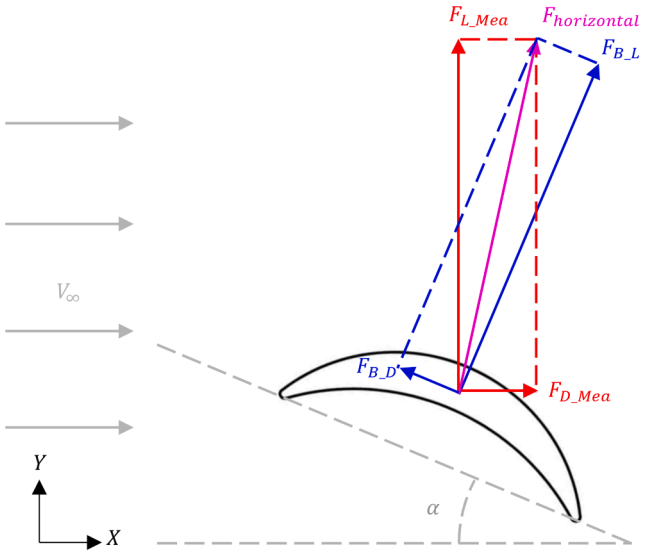


Fig. 8. Schematic of aerodynamic force components in the wind-tunnel coordinate systems.

The forces are measured along three axes: balance lift force (F_{B_L}), balance drag force (F_{B_D}), and balance side force (F_{B_S}). Fig. 8 shows the schematic of the measured force components. Since the external balance rotates together with the wingsail when adjusting α, the direction of F_{B_L} is always perpendicular to the chord line, while F_{B_D} is always in the chordwise direction. It needs to be noted that the positive direction of F_{B_D} points from the leading edge to the trailing edge, so F_{B_D} has a negative value in Fig. 8. F_{B_S} is always in the spanwise direction, *i.e.*, vertical direction. On the other hand, from the aerodynamic perspective, the total horizontal force is divided into another two components: measured lift force (F_{L_Mea}) and measured drag force (F_{D_Mea}), as illustrated in Fig. 8. In the WT tests, F_{L_Mea} and F_{D_Mea} are calculated by Eqs. (6) and (7), respectively.

$$F_{L_Mea} = F_{B_L}\cdot\cos\alpha - F_{B_D}\cdot\sin\alpha \tag{6}$$

$$F_{D_Mea} = F_{B_L}\cdot\sin\alpha + F_{B_D}\cdot\cos\alpha \tag{7}$$

The balance is nulled before each measurement, ensuring that the total measured forces are zero before each trial. The drift of zero is checked after each trial and is in the order of magnitude of 10^{-1} N, and the nulling error in the balance is negligible given the forces involved ($10^1 \sim 10^2$ N). Besides, though the mounted wingsail has vibrations during tests, these minor vibrations of the wingsail do not impact the accuracy of the measurements.

2.2.3.2. Pressure and flow velocity measurement. For measuring the total pressure, a Pitot probe is positioned upstream of the test model, while another is placed downstream within the wake generated by the model. An automated traversing system, controlled by LabVIEW, is used to move the downstream Pitot tube to the required positions during the tests. The pressure measurement uncertainty is ±5 Pa, *i.e.*, < ±0.5% for the pressure coefficient (C_p).

Hot-wire anemometer sensors are employed to measure the flow velocity. These sensors use a tungsten wire that is 1 mm in length and 5 μm in diameter. The hot-wire operates with an overheat ratio of 1.7.

2.2.4. Correction, verification, and uncertainty analysis

2.2.4.1. Boundary layer flow on WT floor. Two perspectives of wall interference are considered: the boundary layer flow of the WT floor and the blockage effect [44]. The measured momentum thickness is less than 5 mm and the measured boundary layer thickness on the WT floor is less than 25 mm. Similar values were also documented by other studies

within the same WT [45]. A theoretical estimation based on Eq. (8) [46] also suggests similar boundary layer thickness on the WT floor, where X is the distance downstream from the start of the boundary layer, *i.e.*, the start of the WT test section. In CFD simulations (details in Sections 2.3 and 3.2.2), the velocity profiles at $X = -7.5L_c$, $-5L_c$, and $-2.5L_c$ are recorded, as shown in Fig. 9, confirming that the boundary layer thickness on the WT floor is less than 25 mm. Since the boundary layer on the WT floor is no thicker than 3% of H, its influence on the wingsail aerodynamic loads is neglected in this study, *i.e.*, the inlet velocity profile is assumed to be uniform.

$$\delta_{99}(X) \approx 0.37 \frac{X}{Re_X^{0.2}} \tag{8}$$

To further assess the potential influence of the WT floor boundary layer, additional post-processing of the CFD simulations is carried out. As shown in Fig. 10, a distinct horseshoe vortex forms at the junction between the wingsail and the floor. Nevertheless, the CFD results indicate that the presence of this vortex has only a limited impact on the global flow field and the aerodynamic loads. According to CFD simulations, the changes in C_L and C_D due to the floor boundary layer remain below 2%, which is within the overall measurement uncertainty.

2.2.4.2. Correction for blockage effects. Since the physical presence of the wingsail model reduces the cross-sectional area of the WT test section, an acceleration of the airflow around the model is induced, *i.e.*, the solid blockage. The blockage ratio, *i.e.*, the ratio between the frontal area of the wingsail models (A_F) and the streamwise sectional area of the WT test section (A_{WT}) varies with α. For a single wingsail model, the blockage ratio is from 1.59% ($\alpha = 0°$) to 4.97% ($\alpha = 90°$).

CFD simulations are conducted to further assess the blockage effects under different boundary assumptions, as illustrated in Fig. 11. In the open-area domain (Fig. 11(a)), which is applied in previous studies regarding full-scale wingsail performance [11,12,23], the wake expands freely without wall confinement. In the slip-wall test-section domain (Fig. 11(b)), the flow is partially constrained, leading to an accelerated jet near the wingsail and reduced expansion of the around-tip flow. In the no-slip test-section domain (Fig. 11(c)), which best represents the physical WT conditions, the blockage effect is most pronounced, with stronger flow acceleration around the wingsail and an upward deflection of the around-tip flow. CFD results indicate that the blockage effects may cause $\sim$ 4% overestimation in force coefficients for $\alpha \sim 15°$, which needs to be corrected.

The blockage effects can be corrected by introducing the blockage correction coefficient [47]. Then the corrected force coefficients, *e.g.*, the corrected drag force coefficient (C_D), can be obtained by Eq. (9). In the same way, the corrected lift force coefficient (C_L) can be calculated. Therefore, for a single full-expanded wingsail with $\alpha = 90°$, the force coefficients are overestimated by approximately 9.7%, while for the triple wingsail system with $\alpha = 20°$, as tested in this study, the overestimation is around 10.1%. In Section 3, unless otherwise specified, the corrected force coefficients are considered.

$$C_D = \left(1 - \frac{A_F}{A_{WT}}\right)^2 \cdot C_{D_Mea} \tag{9}$$

2.2.4.3. Cross-measurement verification. Four sets of verifications of measurement consistency are conducted in this study. The first verification included before- and after-check of both 6-component balances by applying known loads. The second verification is the cross-check of the aerodynamic forces measured by the two balances. The third verification is a cross-check of consistency between the integral aerodynamic pressure load and the lift force. The fourth verification is a cross-check of consistency between the momentum deficit in the wake and the drag force. All sets of verifications revealed very satisfactory results, supporting the conclusion that the measurements in this study are reliable and have acceptable errors.

2.2.4.4. Uncertainty analysis. In addition to the verification procedures described above, an uncertainty analysis was carried out for the force measurements. As each condition was acquired as a long, steady record ($\frac{t_{record}}{L_c/V_\infty} > 10^5$) after transients decayed, the statistical uncertainty is not considered when reporting the time-averaged forces. As mentioned in Section 2.2.3.1, the accuracy of the external balances was ±0.1 N, and the observed zero-drift during the tests was on the order of 10^{-1} N, compared with total aerodynamic forces of 10^1–10^2 N. This corresponds to less than 1% relative errors in the measured total force, and less than 5% in the measured lift and drag forces. Repeated measurements at selected conditions (*e.g.*, $\alpha = 15°$, $Re = 3.6 \times 10^5$) showed variations of less than 1%. Besides, the angle of attack uncertainty is ±0.1° due to mounting tolerance, which is considered not to have significant impacts on the results. Moreover, a previous study used digital image correlation (DIC) methods to record the motions of the wingsail tip during WT tests. It was found that for this solid aluminum wingsail model, the tip motion amplitude is $\sim 10^{-3}$ m, at frequencies around 30–40 Hz. Due to such a small amplitude, the vibration is considered not to affect the accuracy of the mean force measurements.

Overall, the combined uncertainties are often smaller than the symbol size in the presented plots (Fig. 14) and do not affect the interpretation of the aerodynamic characteristics.

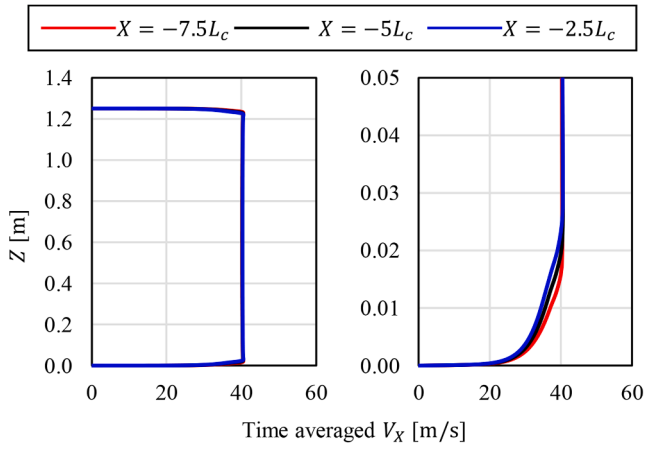


Fig. 9. Triple-wingsail CFD simulation results of the velocity profiles at $\boldsymbol{Y} = 0$, $= -7.5\boldsymbol{L_c}$, $-5\boldsymbol{L_c}$, and $-2.5\boldsymbol{L_c}$. $\boldsymbol{\beta} = 90°$, $\boldsymbol{\alpha} = 20°$ for all three wingsails. $\boldsymbol{V_\infty} = 40\ \mathbf{m/s}$, $\boldsymbol{Re} = 3.6 \times 10^5$.

2.3. CFD simulation

As mentioned in Section 1, a three-dimensional unsteady CFD simulation is performed for visualizing the flow field induced by the single- and triple-wingsail system. The physical conditions in the CFD simulation follow the data mentioned in Section 2.2.1. The simulation adopts the same wingsail model as in the WT tests.

For the triple-wingsail arrangement, the condition with $\alpha = 20°$ and $\beta = 90°$ is selected for the CFD simulation. These angles were chosen because $\alpha = 20°$ corresponds to the angle of attack where the maximum lift coefficient of the crescent profile occurs, making it a representative operational condition for wingsail propulsion. Meanwhile, $\beta = 90°$ represents the apparent wind angle at which the triple-sail configuration generates the maximum total lift, thereby providing the most illustrative case for analyzing the flow mechanisms. The inlet wind speed of 40 m/s is applied.

It should be noted that the CFD simulations in the present study are used as a complementary tool to support the interpretation of the experimentally observed aerodynamic behavior. All quantitative conclusions are primarily based on wind-tunnel measurements, while the

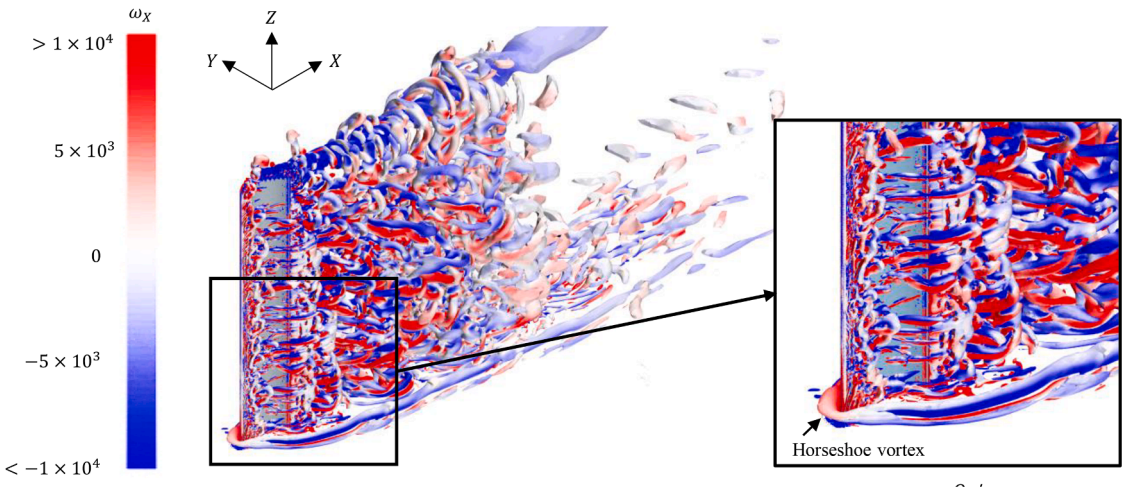


Fig. 10. Single-wingsail CFD simulation results of streamwise vorticity distribution on the isosurface of $\boldsymbol{Q}/\left(\frac{\boldsymbol{V}_\infty}{\boldsymbol{L}_c}\right)^2 = 10$. $\boldsymbol{\alpha} = 15^\circ$. $\boldsymbol{V}_\infty = 40$ **m**/**s**, $\boldsymbol{Re} = 3.6 \times 10^5$.

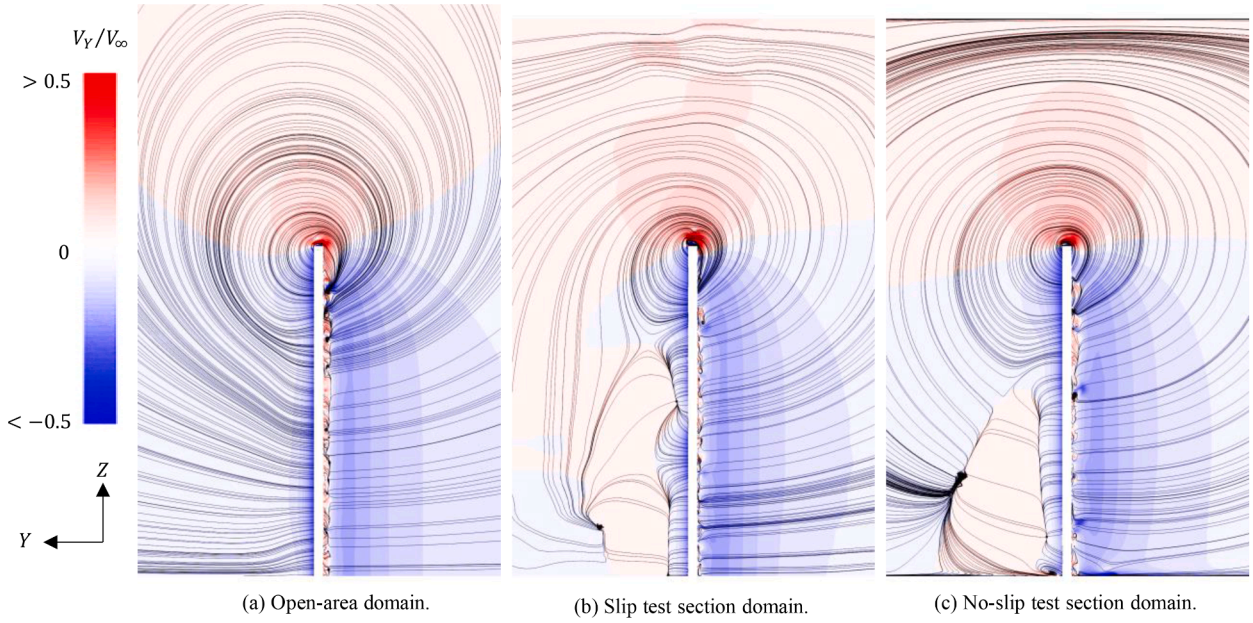


Fig. 11. Single-wingsail CFD simulation results of $\boldsymbol{V_Y}$ distribution and constrained streamlines on the section plane of $\boldsymbol{X} = 0$. $\boldsymbol{\alpha} = 15^\circ$. $\boldsymbol{V}_\infty = 40$ **m** /**s**, $\boldsymbol{Re} = 3.6 \times 10^5$.

CFD results provide physically consistent flow-field information, including separation patterns and wake interactions, which help explain the underlying mechanisms. The CFD predictions have been cross-checked against experimental force coefficients under wind-tunnel-matched conditions (Section 3.2.1), showing consistent trends. Although direct flow-field measurements, *e.g.*, particle image velocimetry (PIV), are not available for pointwise validation, the agreement in global aerodynamic quantities provides confidence in the qualitative reliability of the computed flow structures.

2.3.1. Computational domain and boundary conditions

In previous studies regarding full-size wingsails [11,12,23], a large cuboid computational domain with open boundaries was used in CFD simulations to represent practical sailing conditions. In the present study, however, the CFD domain is modified to replicate the geometry of the closed test section in the wind tunnel in order to enable a direct comparison with the experiments. The cross-sectional dimensions and boundary conditions of the revised triple-wingsail CFD domain are illustrated in Fig. 12. No-slip conditions are applied on the wingsail surfaces and the test-section walls. The upstream panel is set as a velocity inlet, and referring to another study within the same WT [45] and empirical estimations [48], the turbulence intensity and viscosity ratio at the inlet are set to 0.003 and 3, respectively. The downstream panel is set as a pressure outlet, with a relative static pressure of 0.

2.3.2. Turbulence modeling

Building on the method development from a previous study [12], the improved delayed detached eddy simulation (IDDES) approach [49], which integrates Unsteady Reynolds-averaged Navier–Stokes equations (URANS) with large eddy simulation (LES), is used in the CFD simulations. This method enhances the resolution of flow separation caused by the camber [50]. For the regions resolved by URANS, the k–ω SST model [51] is employed.

A blended wall treatment approach [52] is implemented in the URANS model, offering advantages of handling complex geometries with local flow characteristics. Instead of maintaining consistent

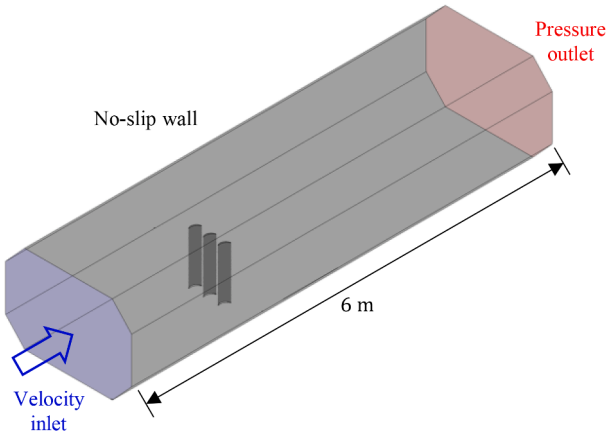


Fig. 12. Computational domain and boundary conditions of the triple-wingsail CFD simulation. $\beta = 90°$, $\alpha = 20°$ for all three wingsails.

dimensionless wall distance (y^+) values in all cells near the walls, which is challenging due to the wide variation in velocity across the curvature wall, this treatment blends wall laws to smoothly capture the changes in the buffer layer between the viscous sublayer and the logarithmic region. The wall function in this approach uses the Reichardt law [53].

2.3.3. Discretization schemes and solvers

A finite volume method (FVM) is applied to discretize the governing equations. The convection fluxes on the cell faces are discretized using a hybrid second-order upwind and bounded-central scheme (hybrid-BCD) [54,55]. The diffusion fluxes are discretized using a second-order scheme. For gradient computation, the second-order hybrid Gauss–LSQ method [54] is employed, which reconstructs field values on the cell. The time derivative is discretized using a second-order implicit method, and the time-marching procedure involves 10 iterations per time step.

A segregated flow solver that employs the semi-implicit method for pressure-linked equations (SIMPLE) algorithm [56] is used. The commercial software Siemens STAR-CCM+ (Siemens PLM [57]) is utilized for conducting the CFD simulations.

2.3.4. Numerical mesh

Nikmanesh [10]; Zhu et al. [23]; Zhu, Yao, et al. [12]; Zhu, Yao, et al. [11] carried out the verification of CFD methods for crescent-shaped wingsails, including mesh independence studies. The mesh topology, mesh refinement strategy (local refinement arrangement), and mesh refinement levels (mesh sizes) were examined. Since those previous studies were performed at higher *Re*, where flow features are more sensitive to mesh and time-step resolution, the adopted criteria are conservative for the present moderate-*Re* cases. Moreover, the turbulence model, discretization schemes, and solver settings are identical to the verified setups in those previous studies. Therefore, no additional mesh-independence study is repeated here, and the present resolution can be considered adequate for capturing the aerodynamic characteristics discussed in this study.

The trimmed cell topology (unstructured) is utilized for mesh generation, as illustrated in Fig. 13. The cells maintain a uniform size within each region at every refinement level. Refinements are applied to the region near the foils and the wake region, which is presented in the section plane at $Z = 0.5H$ in Fig. 13(b) and (c). Due to the presence of large flow gradients around the two edges, a finer mesh is also applied to the regions near the foil edges, as depicted in Fig. 13(d). Additionally, the mesh around the wingsail top tip is refined to better capture the tip vortices.

Prism layer cells are generated near the wingsail wall to resolve the boundary layer flow. Following the methods developed by Zhu, Yao, et al. [11], the total thickness of the prism layer on the wingsail's wall is set to 5×10^{-3} m, and the number of prism layers is 55, as depicted in Fig. 13(d). A criterion of $y^+ \sim 10^{-1}$ is met in most areas of the wall,

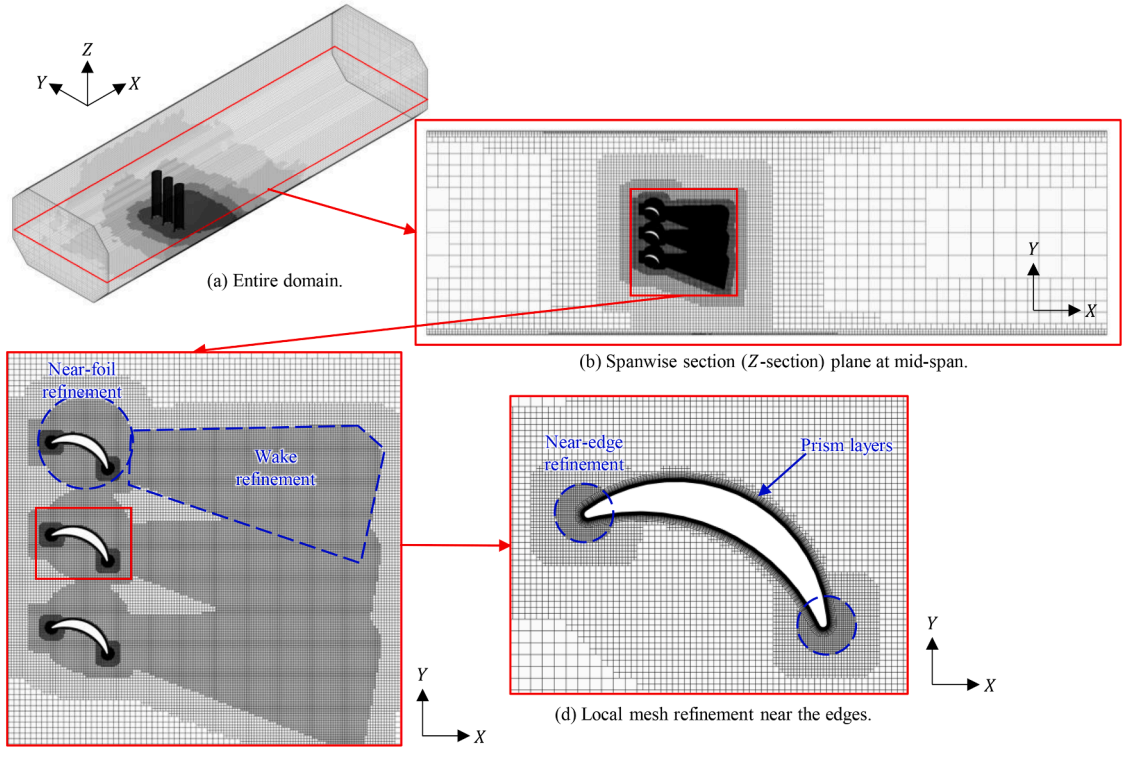


Fig. 13. Numerical mesh for the triple-wingsail CFD simulation. $\beta = 90°$, $\alpha = 20°$ for all three wingsails.

because it is important for the y^+ value of the first layer of cells near the wall to be <1 to ensure a more detailed and accurate analysis of the boundary layer flow. Thus, the near-wall thickness of the prism layer is set to 2 $\times 10^{-7}$ m. The entire mesh contains approximately 63 million cells.

3. Results and discussion

3.1. Single-wingsail aerodynamic performance

3.1.1. Critical Re

First, the wingsail model of the larger aspect ratio (5.3) is tested. The lift and drag force coefficients, C_L and C_D of the single foil with boundary layer tripping are shown in Fig. 14. Five sets of V_∞ within the range from 20 m/s to 40 m/s are tested, *i.e.*, *Re* is in the range from 1.8 $\times 10^5$ to 3.6 $\times 10^5$. In the single-wingsail WT tests, α range is from 0° to 90°.

A previous study [12] performed full-scale CFD simulations for the same crescent-shaped wingsail ($Re = 7.1 \times 10^6$). In the present study, additional comparisons between WT measurements (without correction for blockage effect), model-scale CFD, and full-scale CFD [12] are provided in Fig. 15. As the difference is less than 2%, the agreement among the three datasets confirms the reliability of the force coefficients obtained from the simulations and demonstrates that scale effects are limited for this geometry when proper tripping is applied. This study therefore provides the first experimental validation of the aerodynamic coefficients of crescent-shaped wingsails, and establishes a consistent link between model-scale and full-scale predictions.

It should be noted that compared with conventional airfoils (*e.g.*, NACA series), the maximum lift coefficient, $C_L \approx 2$, is unusually high. As mentioned in Section 1, this difference is because of the design philosophy: conventional airfoils are optimized for applications such as aircraft wings or turbine blades, where minimizing drag is critical and hence a high lift-to-drag ratio (C_L/C_D) is targeted. In contrast, for ship wingsails, F_D can also contribute positively to thrust under certain wind conditions, so the design emphasis is placed on achieving high C_L rather than maximizing C_L/C_D. The crescent-shaped profiles therefore employ a much larger camber than conventional airfoils, which sustains strong suction on the upstream suction side and leads to the elevated lift levels observed here.

As can be seen in Fig. 14(a), from the perspective of force coefficients, the three cases with low *Re* from 1.8 $\times 10^5$ to 2.7 $\times 10^5$ show similar results. However, when *Re* varies from 2.7 $\times 10^5$ to 3.1 $\times 10^5$, C_L at 10° $\leq \alpha \leq$ 25° notably increases, while C_D decreases. For instance,

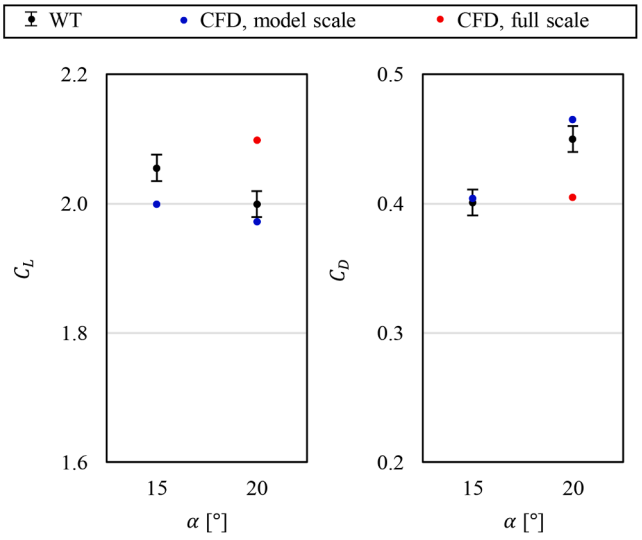
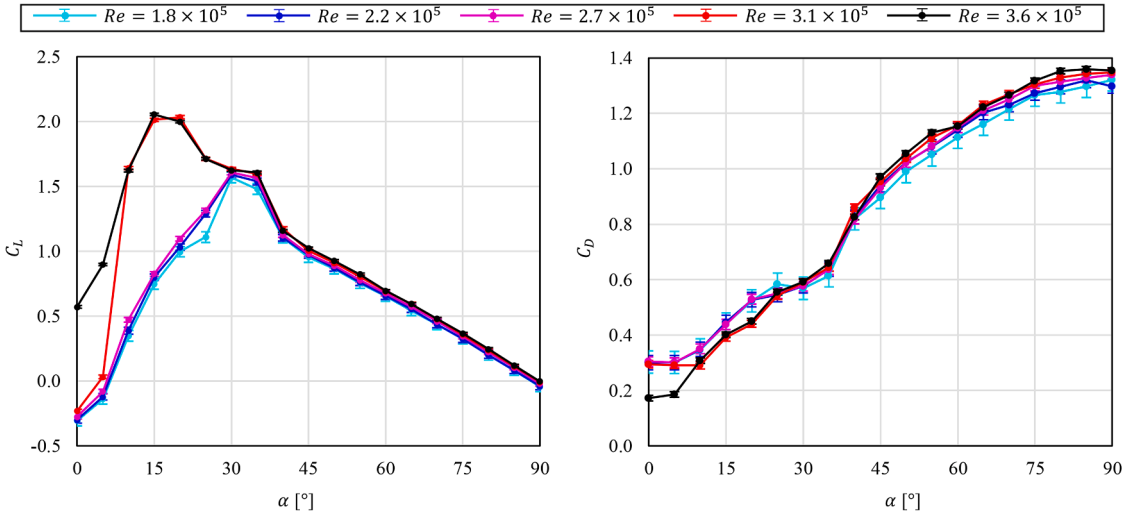


Fig. 15. Single-wingsail force coefficients comparison among WT tests, model-scale and full-scale CFD simulations.

C_L at $\alpha = 15°$ increases from 0.83 to 2.01. Meanwhile, for α in the range from 0° to 5°, the large changes of force coefficients occur between $Re = 3.1 \times 10^5$ and 3.6 $\times 10^5$. These phenomena were also observed in studies with similar geometries, *e.g.*, Souppez et al. [58] studied flow around an arc and found that C_L at 14° $\leq \alpha \leq$ 20° sharply increases when *Re* varies from 5.4 $\times 10^5$ to 6.8 $\times 10^5$.

The significant changes in the aerodynamic loads due to changes in *Re* are referred to as lift crisis and drag crisis, collectively termed a force crisis [59,60], a common phenomenon for blunt bodies like cylinders [61]. The major reasons for the force crisis are the laminar-turbulent transition and flow separation [62]. According to relevant studies regarding airfoils with a large camber [63,64], when *Re* varies, the flow pattern on the suction side can undergo three stages: laminar separation with laminar reattachment, laminar separation with turbulent reattachment, and turbulent separation with turbulent reattachment. In this study, as discussed in Section 2.2.3, the maximum inlet turbulence intensity is within 0.1%, which indicates the possibility of an initially laminar boundary layer on the foil at small α and low *Re*.

However, Souppez [65] and Zeng et al. [66] focused on arc-shaped sails, indicating that when *Re* exceeds a certain value, the force



(a) C_L *vs.* α. (b) C_D *vs.* α.

Fig. 14. Single-wingsail WT test results of the aerodynamic force coefficients of the fully expanded wingsail at different $\boldsymbol{\alpha}$ and ***Re***.

coefficients show limited sensitivity to *Re*. In practice, the full-size wingsail is expected to be operated under a much higher *Re*, *e.g.*, 1×10^7, so for full-size wingsails, the force coefficients are not so sensitive to *Re*. Therefore, this study does not go deeper into the laminar-turbulent flow transition of the wingsail with crescent-shaped profiles, but a fine-step *Re* sweep and transition-sensitivity study (including the *Re* dependence of flow separation and reattachment patterns) has been carried out in a parallel work [67], where these mechanisms are analyzed in detail.

Some studies have indicated that the leading edge separation bubble (LESB) [68] might also be one of the reasons for the force crisis [58,69]. The LESB is a small region of separated flow that occurs near the leading edge of airfoils, particularly at low *Re*. However, these studies are conducted based on geometries with very sharp leading edges. Besides, the LESB was not observed in previous studies regarding the same geometry in full scale based on URANS and IDDES CFD simulations [12]. Hence, the effect of LESB is not regarded as one of the major reasons for the *Re* sensitivity of aerodynamic loads in this study.

3.1.2. Stall and critical angle of attack

In Fig. 14(a), the WT test results show that there are two peaks of C_L. For example, when $Re = 3.6 \times 10^5$, two peaks of C_L can be found at $\alpha \approx 15^\circ$ and 35°, respectively. To interpret the force measurements and have a deeper insight into the aerodynamic loads on the wingsail, the pressure distribution on the wingsail is measured. The measurement takes place at the midspan, $Z = 0.5H$, of an airfoil section with $H = 0.26$m, and the distribution of C_p is plotted in Fig. 16.

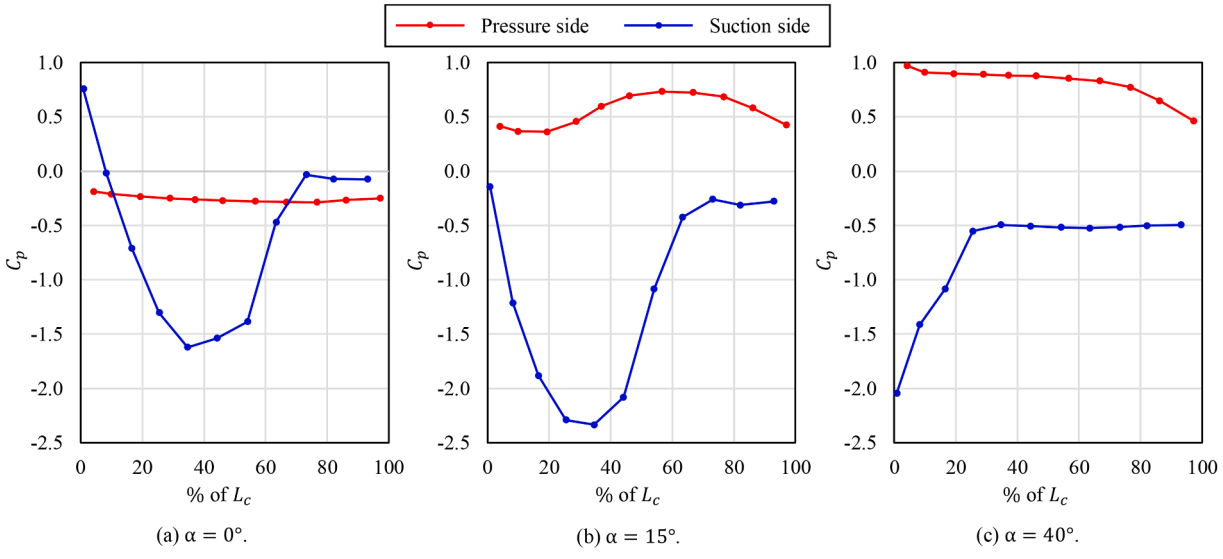
As Fig. 16(a) shows, at $\alpha = 0^\circ$, the pressure on the pressure and suction sides of the wingsail shows an inverted sign at both the leading and trailing edges. Besides, due to the flow separation induced by the leading edge at small α [11], the pressure is negative on the pressure side. The pressure difference between the two sides of the wingsail is smaller at $\alpha = 0^\circ$ than that at $\alpha = 15^\circ$ or 40°, leading to low C_L at $\alpha = 0^\circ$. At $\alpha = 15^\circ$, where the highest C_L is achieved during the WT tests, the pressure on the upstream half of the suction side is very low, as shown in Fig. 16(b), causing a strong suction force. According to numerical simulation results presented by Zhu, Yao, et al. [12]; Zhu, Yao, et al. [11], the high-velocity flow on the suction side is the core reason. The location of stall from pressure measurements is identified by a plateau with constant pressure. The pressure inside a separation bubble is constant. In Fig. 16(a) and (b), the constant pressure is achieved at 70%. However, in Fig. 16(c), it is found that at $\alpha = 40^\circ$, where C_L is close to C_D, the stall is located at 25% chord. Low pressure occurs on the suction side close to the leading edge, which contributes to F_L and also causes a moment on the wingsail. Study by Zhu, Yao, et al. [11] confirms this observation. For angles of attack between 0° and 15°, the stall location is fixed at 70% chord, and for angles of attack between 15° and 40°, the stall location gradually moves upstream from 70% chord to 25% chord. The variation in lift performance (Fig. 14(a)) can be explained by the variation in the stall location, as confirmed by the pressure measurements. The present measurements provide the first experimental validation of the pressure distribution for a crescent airfoil.

Zhu, Yao, et al. [11] studied the force coefficients *vs.* the angle of attack (α) of a similar geometry based on full-scale CFD simulations, which also indicated that the curve of C_L *vs.* α shows two peaks. Robert and Newman [70] conducted WT tests for a cambered sail with a large range of α and also found two peaks of C_L. By analyzing the flow field characteristics, Zhu, Yao, et al. [11] indicated that the reason for both peaks is the low pressure on the suction side due to high-velocity flows. For the first peak with lower α, *i.e.*, the critical angle of attack (α_c) the high-velocity downflow on the suction side leads to the large suction force. However, the second peak occurring after stall with higher α is because of the high-velocity counter-flow on the suction side. However, Zhu, Yao, et al. [11] found that the first peak of C_L happens at $\alpha \approx 20^\circ$, which is higher than the value provided by this study. Similar phenomena have also been detected by Hou et al. [71] when comparing experimental and numerical results of a windsurfing sail. As discussed in Section 3.1.1, the *Re* sensitivity due to laminar-turbulent transition and separation is supposed to be the main reason.

To further interpret the mechanism behind the variation of lift with Reynolds number, Fig. 17 presents the CFD flow fields at $\alpha = 15^\circ$ for $Re = 1.8 \times 10^5$ and 3.6×10^5 cases. At low *Re*, the suction-side boundary layer has early separation, leading to a large separation region and the presence of high-velocity backward flow near the surface. This limits the suction peak and results in a lower C_L. At high *Re*, the boundary layer transitions earlier to turbulence and reattaches more effectively, sustaining a high-velocity forward jet over the suction side. The enhanced suction explains the sharp rise of C_L observed in Fig. 14 and the occurrence of the first lift peak, as shown in Fig. 17.

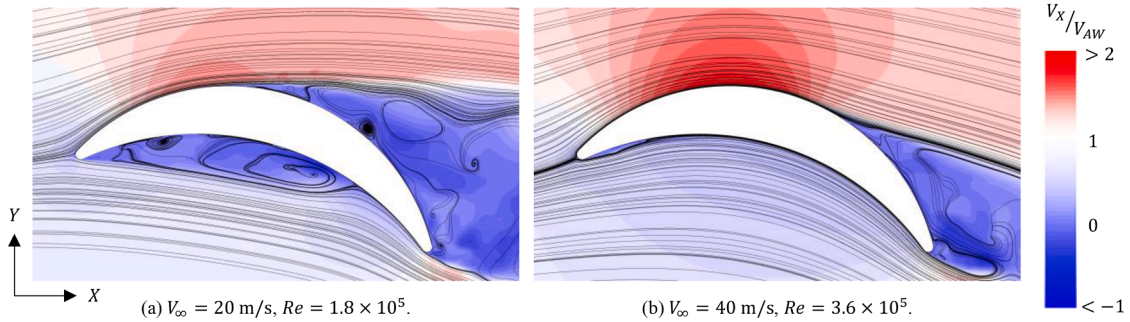
3.1.3. Aspect ratio sensitivity

As discussed in Section 2.1.2, the wingsail can be either expanded or retracted under different wind conditions. In this study, the semi-retracted and fully expanded conditions are tested in the WT. The height, *H*, is 0.74 m for the large aspect ratio, $AR = 5.3$, and 0.50 m for the small aspect ratio, $AR = 3.6$. The measured force coefficients at



(a) α = 0°. (b) α = 15°. (c) α = 40°.

Fig. 16. Single-wingsail WT test results of surface pressure distribution of the wingsail model at $\boldsymbol{Re} = 3.6 \times 10^5$, measured at $\boldsymbol{Z} = 0.5\boldsymbol{H}$.



(a) $V_\infty = 20$ m/s, $Re = 1.8 \times 10^5$. (b) $V_\infty = 40$ m/s, $Re = 3.6 \times 10^5$.

Fig. 17. Single-wingsail CFD simulation results of streamwise velocity distribution and constrained streamlines on the section plane of $\boldsymbol{Z} = 0.5\boldsymbol{H}$. $\boldsymbol{\alpha} = 15^\circ$.

three different sets of V_∞ are plotted in Fig. 18.

C_L and C_D of the fully expanded wingsail resemble those of the semi-retracted wingsail at all tested V_∞. Regarding C_L, it is noted that the lift coefficient in Fig. 18 corresponding to the fully expanded wingsail is slightly higher than that of the semi-retracted wingsail. This can be attributed to end effects and tip vortices, which have negative effects on C_L [11,12]. Indeed, the end effects are more significant on the wingsail with a smaller aspect ratio, since a larger proportion of the wingsail is affected by the end effects. Comparison of Fig. 18(d) with the other subfigures indicates that the influence on C_L from tip vortices occurs in a broader range of α for low-Re conditions. Regarding C_D, the retraction of the wingsail causes a minor reduction of the drag coefficient, according to the WT test results shown in Fig. 18.

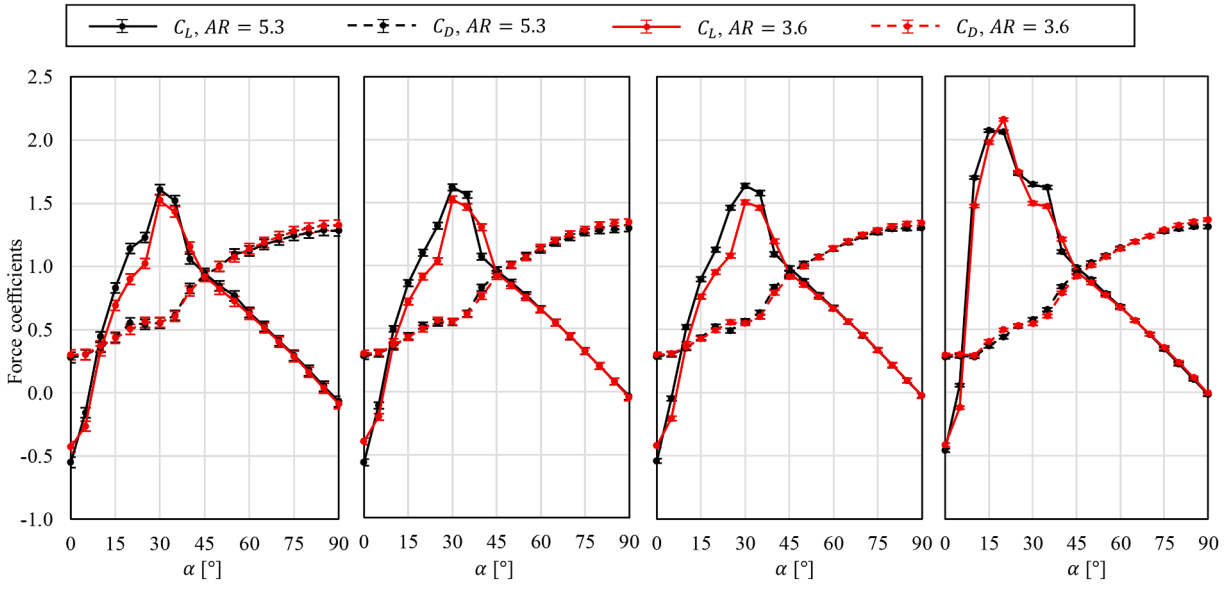
In addition, the classical lifting-line estimates for inviscid wings, where $\Delta C_L/\Delta\alpha = 2\pi AR/(AR+2)$ [34,72]. The theoretical slopes are approximately 5.0 rad^{-1} for $AR = 5.3$ and 4.6 rad^{-1} for $AR = 3.6$. These values are close, which corroborates the experimental results and explains why the difference between the two tested aspect ratios is small.

Apart from the tip effects, which are slightly more significant on the retracted wingsail than on the fully expanded wingsail, the wingsails exhibit similar aerodynamic behaviors. Therefore, the current results clearly show that for the high flow Reynolds number, the force coefficients obtained for a high aspect ratio configuration can be applied with good approximation for a low-aspect ratio configuration, and *vice versa*.

3.1.4. *Unsteady flow features*

To assess the unsteady flow field induced by the wingsail, the velocity downstream of the wingsail at different distances along Y direction is measured by a hot-wire probe. Then, a Fourier analysis is performed in order to deduce the wingsail-induced flow frequencies (f). The tests are performed on a fully expanded wingsail model with $\alpha = 0^\circ$ at $Re = 1.1 \times 10^5$, 1.3×10^5, and 2.2×10^5 ($V_\infty = 12$, 15, and 24 m/s). The case of $\alpha = 0^\circ$ was chosen because it represents a canonical bluff-body shedding condition, where the wake dynamics are dominated by a clear, narrow-band vortex-shedding frequency. This allows an unambiguous identification of the Strouhal number and a reliable extrapolation to full scale. Meanwhile, at higher angles of attack, the flow becomes strongly separated and the velocity spectra are broadband with weak or multiple peaks, making it difficult to extract a consistent characteristic frequency. Therefore, this case provides a representative baseline for assessing the unsteady features.

The frequency domain of the downstream velocities is plotted in Fig. 19, where $A(V_X)$ represents the spectral amplitude of streamwise velocity (V_X). The shedding frequencies, f are 30 Hz, 37 Hz, and 53 Hz, for the three sets of V_∞, respectively. With the hypothesis that the Strouhal number ($St = fL_c/V_\infty$) remains constant for a certain α, a linear regression analysis is carried out for f and V_∞, as shown in Fig. 20. The coefficient of determination, *i.e.*, the R-squared value, is 0.9965, meaning that the regression predictions fit the data very well. Based on this hypothesis ($St = 0.35$ remains constant), f of a full-size wingsail can be estimated. For example, if considering $V_{AW} = 8$ m/s, the estimated f



(a) $Re = 1.8 \times 10^5$. (b) $Re = 2.2 \times 10^5$. (c) $Re = 2.7 \times 10^5$. (d) $Re = 3.1 \times 10^5$.

Fig. 18. Force coefficients of the wingsails with different aspect ratios, based on single-wingsail WT test results.

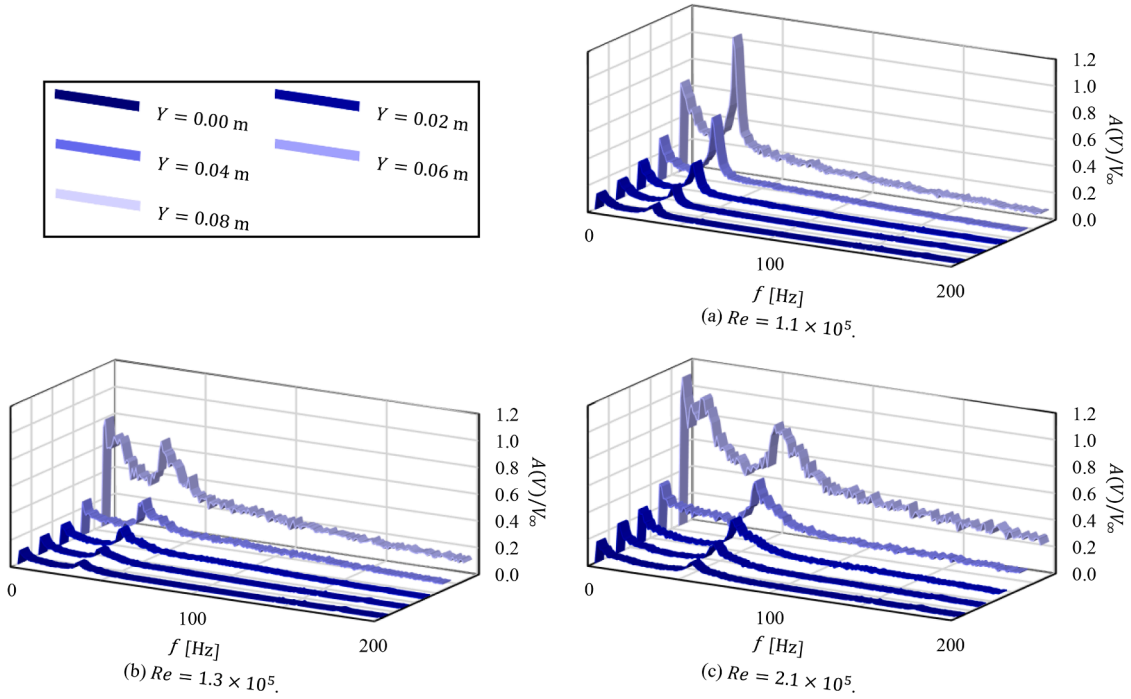


Fig. 19. Frequency spectrum of downstream flow at several positions along the cross-flow direction for a fully expanded wingsail at $\alpha = 0^{\circ}$, based on WT test results.

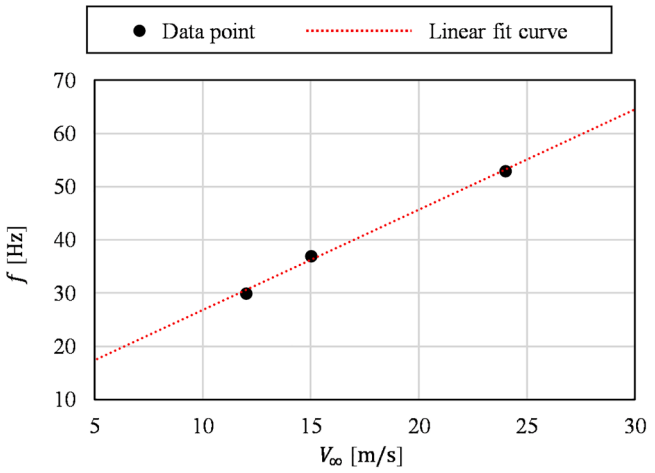


Fig. 20. Linear regression of f *vs.* V_{∞} for a fully expanded wingsail at $\alpha = 0^{\circ}$.

is approximately 0.2 Hz for a full-scale wingsail. Such low frequency is consistent with the very large chord length of a full-scale wingsail, and the same order of magnitude has also been suggested by Zhu [67]; Zhu, Yao, et al. [12]. These wake-unsteadiness data are important for further studies on fluid-structure interactions (FSI). It should be noted that strict Re similarity is not satisfied between model-scale ($Re \sim 10^5$) and full-scale conditions ($Re \sim 10^7$). However, previous scale-resolving CFD studies [12,67] indicate that St varies in the lower Re regime ($Re \approx 1.8 \times 10^5$ –3.6×10^5) due to changes in separation behavior, but becomes relatively insensitive to Re once fully turbulent separation is established ($Re \gtrsim 3.6 \times 10^5$). Therefore, the present estimate should be interpreted as an order-of-magnitude indication of the vortex shedding frequency at full scale, rather than a precise prediction.

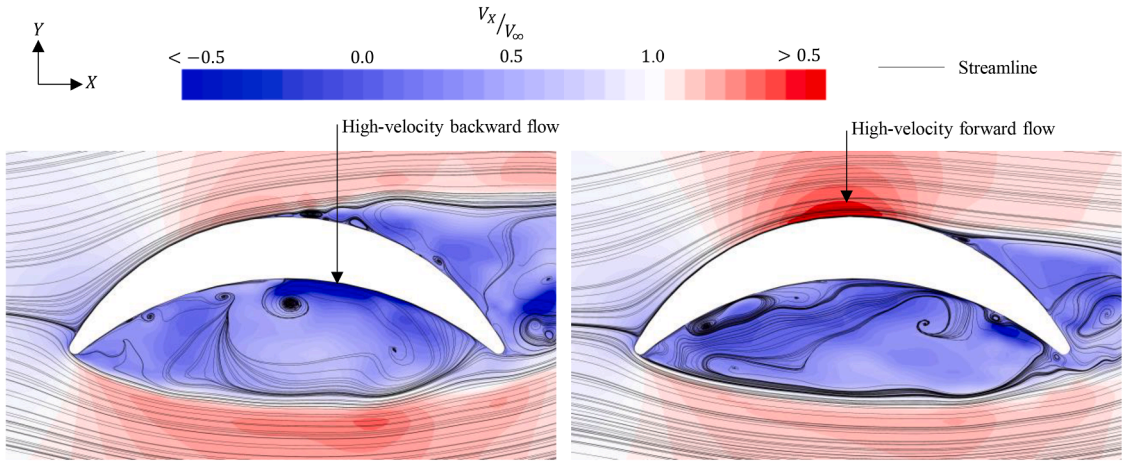
To further interpret the unsteady flow features at $\alpha = 0^{\circ}$, the CFD flow fields are presented in Fig. 21. At low $Re = 1.8 \times 10^5$, a large recirculation region is observed on the pressure side, with a pronounced high-velocity backward flow close to the surface. This separated shear layer sheds periodically into the wake, generating a coherent vortex street and the narrow-band spectral peaks measured in Fig. 19. In contrast, at higher $Re = 3.6 \times 10^5$, the separation bubble is significantly reduced, and a high-velocity forward flow is sustained over the suction side. This leads to a more attached shear layer and a shift in the shedding frequency. The comparison between the two cases highlights that the unsteady signals captured by the hot-wire probes originate from periodic vortex shedding associated with the separation–reattachment cycle, and the sensitivity of these features to Re explains the observed frequency scaling.

3.2. Triple-wingsail interaction

3.2.1. Aerodynamic loads

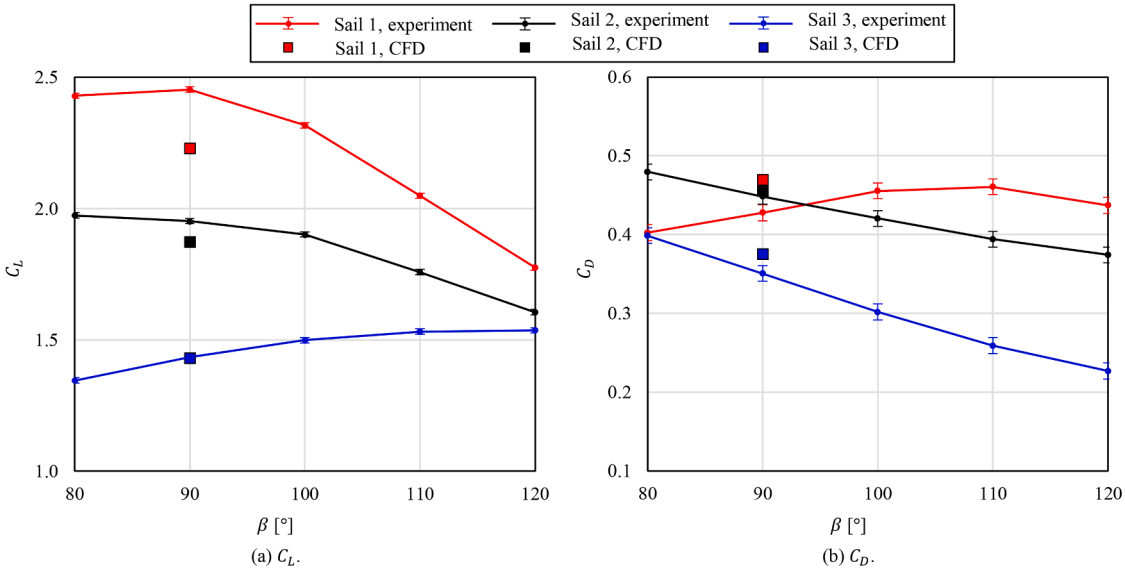
The aerodynamic force coefficients, *i.e.*, C_L and C_D, measured for the triple in-line wingsail system (cf. Fig. 3) at different β and $Re = 3.6 \times 10^5$ are shown in Fig. 22, where all wingsails are angled with $\alpha = 20^{\circ}$. It is seen that Sail 3, *i.e.*, the downstream (stern) wingsail, generates the smallest lift force (F_L) among the three wingsails for $\beta \in [80^{\circ}, 120^{\circ}]$, whereas Sail 1 (bow) generates the largest F_L. For the drag force (F_D), Sail 2 (middle) generates the largest F_D when $\beta \leq 90^{\circ}$, but Sail 1 (bow) generates the largest F_D when $\beta \geq 100^{\circ}$. Sail 3 (stern) always generates the smallest F_D. The differences of force coefficients among the three wingsails indicate that the flow interaction between the wingsails affects the distribution of the aerodynamic loads.

The simulation is performed with the physical condition of $Re = 3.6 \times 10^5$, $\alpha = 20^{\circ}$, $\beta = 90^{\circ}$. This particular yaw angle, β, is chosen, because the total F_L generated by the triple-wingsail system achieves its maximum value at $\beta = 90^{\circ}$. The force coefficients of each wingsail from the CFD simulation show the same trend as those measured from the WT tests. The upstream wingsail generates the highest C_L while the downstream one generates the lowest, as plotted in Fig. 22. However, the lift non-uniformity is predicted more conservatively by the CFD simulation. One contributing reason may be the turbulence tripping in the WT tests, where the boundary-layer transition was triggered by surface tape at $0.1L_c$. In contrast, the CFD simulations employed an IDDES approach without an explicit transition model, effectively assuming a fully



(a) $V_\infty = 20$ m/s, $Re = 1.8 \times 10^5$. (b) $V_\infty = 40$ m/s, $Re = 3.6 \times 10^5$.

Fig. 21. Single-wingsail CFD simulation results of the streamwise velocity distribution and constrained streamlines on the section plane of $\boldsymbol{Z = 0.5H}$. $\boldsymbol{\alpha} = 0°$.



(a) C_L. (b) C_D.

Fig. 22. Force coefficients of the triple-line-up wingsail system at different $\boldsymbol{\beta}$ at $\boldsymbol{Re} = 3.6 \times 10^5$ and $\boldsymbol{\alpha} = 20°$.

turbulent boundary layer from the leading edge. This mismatch can alter separation and reattachment behavior, especially in highly cambered profiles.

3.2.2. *Flow field characteristics*

Fig. 23 illustrates the spanwise development of the flow field around the triple-wingsail system. At the near-root section ($Z = 0.01H$, Fig. 23 (a)), obvious horseshoe vortices (also discussed in Section 2.2.4.1) form at the junction between the sail and the wind-tunnel floor, inducing strong local recirculation.

According to Fig. 23(b)–(i), Sail 1 consistently sustains a well-defined high-speed jet on its suction side, whereas this region becomes weaker on Sail 2 and further diminished on Sail 3. This trend directly explains the significant reduction of C_L from Sail 1 to Sail 3. The interaction between the three sails is also clearly visible: the wake shed from Sail 1 impinges on the suction side of Sail 2, modifying its boundary-layer development, and in turn the wake from Sail 2 affects Sail 3, leading to cumulative losses in suction. This interaction can lead to a phenomenon known as “downwash” where the airflow is pushed downwards behind each sail, affecting the angle of attack and the effective wind speed experienced by the downstream sails [73]. This interaction can affect the lift-to-drag ratio for Sail 2 and Sail 3 which are in the wake of upstream sails, particularly under low-β conditions.

However, though the velocity field is deeply altered by the triple-wingsail interaction, from the perspective of the vorticity, the interaction among the three wingsails is limited, since the vortex tubes induced by each wingsail in the wake are essentially independent, as shown in Fig. 24, where the non-dimensional Q-criterion (the second invariant of the velocity gradient tensor) on the mid-span section is visualized. In terms of flow separation, the sections from Fig. 23(b)–(h) show that the separation point on the suction side gradually shifts downstream with increasing spanwise height, implying that the mid–upper spans contribute most to the overall lift generation for each sail. Taking the mid-span flow as an example (Fig. 23(e)), it can also be found that the starting location of flow separation is closer to the leading edge for Sail 1, compared with Sail 2 and Sail 3. Fig. 24 also suggests that Sail 1 induces the strongest vortex shedding. Sail 2 is intermediate, and the vortex shedding induced by Sail 3 is the weakest.

Similar to the single wingsail flow fields visualized in previous studies [11,12], the streamwise vorticities around the wingsail tips are indicative of strong tip vortices, which are caused by the flow leakage around the tip from the pressure side to the suction side. In Fig. 23(h)

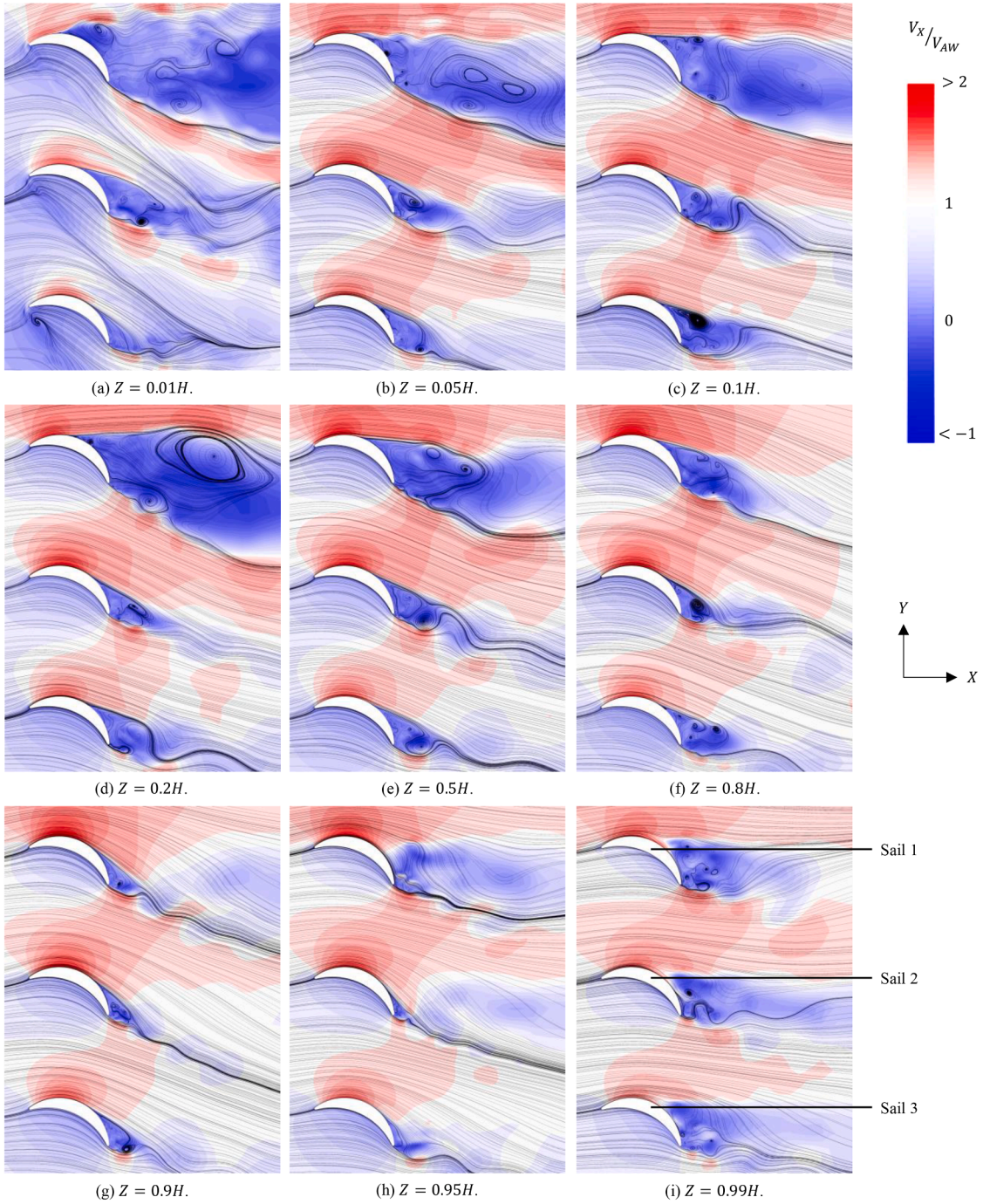


Fig. 23. Triple-wingsail CFD simulation results of streamwise velocity distribution and constrained streamlines on the section planes of various spanwise positions. $\boldsymbol{\beta} = 90^{\circ}$, $\boldsymbol{\alpha} = 20^{\circ}$ for all three wingsails. $\boldsymbol{V}_{\infty} = 40\ \mathbf{m/s}$, $\boldsymbol{Re} = 3.6 \times 10^5$.

and (i), strong tip vortices are evident near the tip. Although the flow becomes attached over much of the suction surface and the nominal separation point is located far downstream, the tip-around flow (also discussed in Section 2.2.4.2) reduces the streamwise flow velocity, weakening the suction force, and preventing the formation of strong lift near the tips. These tip vortices can induce additional drag, which can cause negative effects on the propulsive performance of wingsails when $\beta \leq 90^{\circ}$ by reducing the effective F_T generated. In a triple-line configuration, the interaction of these vortices becomes even more complex, especially under low-β conditions, as they can interact with adjacent wingsails, potentially affecting the flow field experienced by each sail.

3.3. Propulsive performance prediction

3.3.1. Thrust and operation strategy

Contrary to an airplane, where minimizing drag is desired, for wingsails on ships, the objective is to determine the pair of angles (α and β) that maximize F_T [12]. According to the principles of sailing described in Section 2.1.1, the thrust coefficient C_T of a single wingsail can be derived as a function of α and β using Eq. (3). Based on the force coefficients at $Re = 1.8 \times 10^5$ and 3.6×10^5 obtained from the experimental results in Fig. 14, the corresponding C_T values for β between 0° and 180° are evaluated and presented in Fig. 25. The red contours represent positive C_T, while the blue contours represent negative values

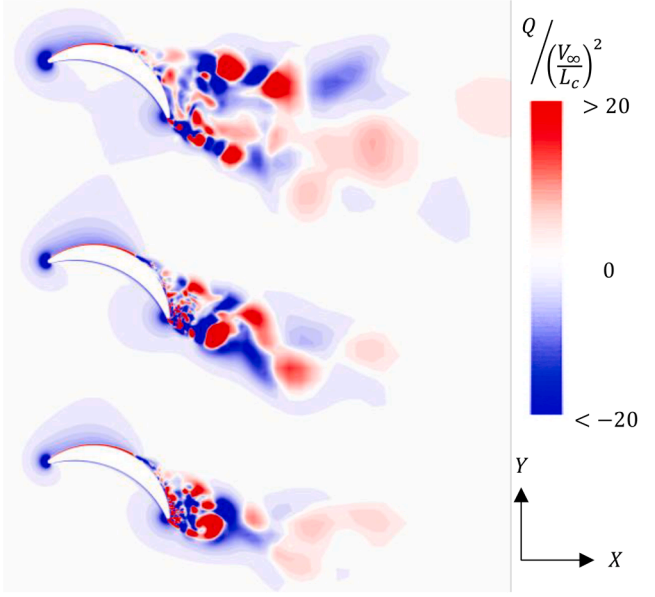


Fig. 24. Triple-wingsail CFD simulation results of distribution of $\boldsymbol{Q}/\left(\frac{\boldsymbol{V}_\infty}{\boldsymbol{L}_c}\right)^2$ on the section planes of $\boldsymbol{Z} = 0.5\boldsymbol{H}$. $\boldsymbol{\beta} = 90^\circ$, $\boldsymbol{\alpha} = 20^\circ$ for all three wingsails. $\boldsymbol{V}_\infty = 40\ \mathbf{m/s}$, $\boldsymbol{Re} = 3.6 \times 10^5$.

meaning that the wingsail does not contribute to propulsion but generates extra resistance to the ship. The wingsail is recommended to be operated at α where the maximum C_T is achieved at each value of θ_{AW}. Hence, the results for the propulsive performance, *i.e.*, the highest C_T at different θ_{AW}, are plotted in Fig. 26(a). The wingsail operation strategy, *i.e.*, α that is applied to obtain the highest C_T, is plotted in Fig. 26(b). The contributions to the thrust of the force components, *i.e.*, the lift-to-drag ratio, are plotted in Fig. 26(c). Only half of the polar plot, *i.e.*, $0^\circ \leq \theta_{AW} \leq 180^\circ$, is presented, since it is always symmetric.

For θ_{AW} lower than 20°, *i.e.*, the sailing vessel is navigating against the wind, it is not possible to achieve positive thrust, so the wingsail will be counterproductive. This phenomenon has been indicated in a previous study for a similarly shaped crescent wingsail [11]. This point of sail is called the "no-go zone" where a sailing craft may be "in irons" [74]. In the analysis shown in Fig. 26, for $\beta = 0^\circ$, the maximum C_T occurs at $\alpha = 0^\circ$ in order to minimize the drag induced by the sail, but in practice, the wingsail is usually reefed to avoid the negative thrust under headwind conditions.

For θ_{AW} between 30° and 150°, the maximum C_T is found at $\alpha = 30^\circ$ and $\alpha = 15^\circ$ according to the dataset of $V_\infty = 20$ m/s and 40 m/s, respectively. F_L mainly contributes to the thrust within this range of θ_{AW}, so the wingsail is operated at α with the highest C_L, *i.e.*, α_c. This operation strategy was also pointed out by Zhu, Yao, et al. [11]. For θ_{AW} greater than 155°, the maximum C_T occurs at $\alpha \approx 80^\circ$ with F_D mainly contributing to the thrust. The propulsive performance under downwind conditions is not as good as that under side wind conditions.

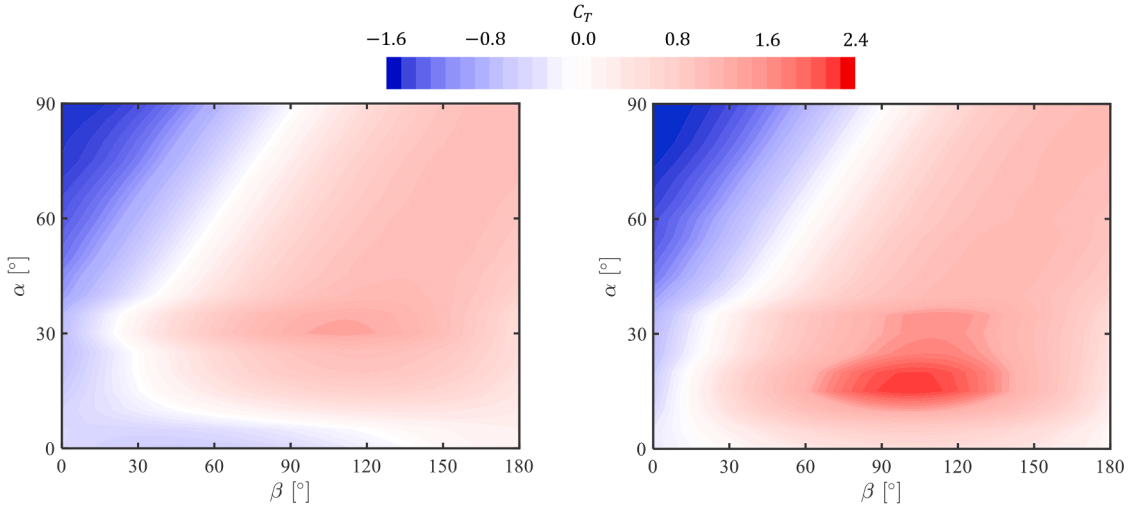
As discussed in Section 3.1.1, the results based on 40 m/s are more representative of the practical situation. Predicting the propulsive performance based on experimental tests with low *Re* may suggest an inappropriate α and underestimate C_T.

It should also be noted that according to Zhu, Yao, et al. [11], when θ_{AW} is between 120° and 150°, the wingsail should be operated with $\alpha \approx 40^\circ$ where $C_L \approx C_D$. However, in this study, this situation only happens in a very small range of θ_{AW} from 150° to 155°, when considering force coefficients based on $V_\infty = 40$ m/s. The reason is the difference in wingsail geometries. The crescent-shaped profile considered in this study was optimized by Zhu, Yao, et al. [75] to have a larger camber hence leading to a higher C_L, compared with that studied by Zhu, Yao, et al. [11], so that F_L plays a more important role in propulsion.

According to the force coefficients of the triple-wingsail configuration shown in Fig. 22, C_T *vs.* θ_{AW} for each wingsail can also be calculated and plotted, as shown in Fig. 27. Since the upstream wingsail provides the highest C_L, it also contributes to the ship propulsion most. If considering the mean value of C_T of the three wingsails, the highest $C_T = 1.92$ is obtained at $\theta_{AW} = 90^\circ$, which is slightly lower than that of a single wingsail ($C_T = 2.11$). As Fig. 27 shows, the thrust of the Sail 2 is very close to the mean thrust of the sail system and the thrust decrease on Sail 3 is compensated by the thrust increase on Sail 1.

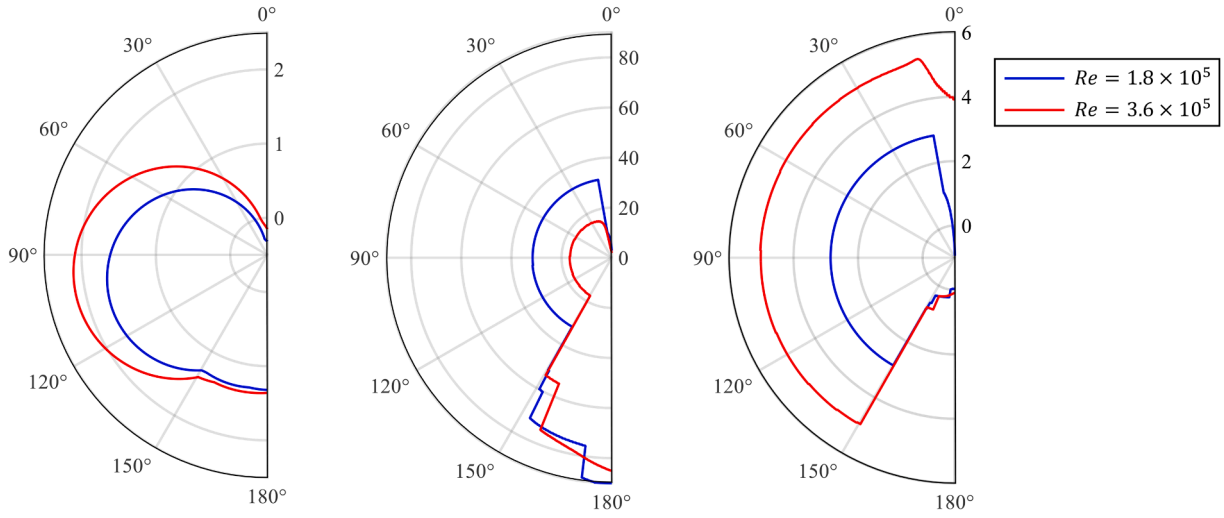
3.4. Side force effects

Wind loads on wingsails may have an influence on the static and dynamic behaviors of ships. In this analysis, a general Panamax oil tanker is used as a case study, with its main dimensions and parameters listed in Table 1. The propulsive performance of a triple-wingsail system and its effects on the ship's statics are discussed. For instance, under the side wind condition ($\theta_{AW} = 90^\circ$) with $V_{AW} = 8$ m/s, the thrust force (F_T) and side force (F_S) generated by the full-expanded triple-wingsail system are approximately 2.3×10^5 and 4.4×10^4 N, respectively, as



(a) According to force coefficients at $Re = 1.8 \times 10^5$. (b) According to force coefficients at $Re = 3.6 \times 10^5$.

Fig. 25. C_T *vs.* $\boldsymbol{\alpha}$ and $\boldsymbol{\beta}$, based on fully expanded single-wingsail WT tests with different $\boldsymbol{V}_\infty$.



(a) C_T *vs.* θ_{AW}. (b) α *vs.* θ_{AW}. (c) C_L/C_D *vs.* θ_{AW}.

Fig. 26. Polar diagrams of C_T, α, and C_L/C_D *vs.* θ_{AW}, based on fully expanded single-wingsail WT tests with different *Re*.

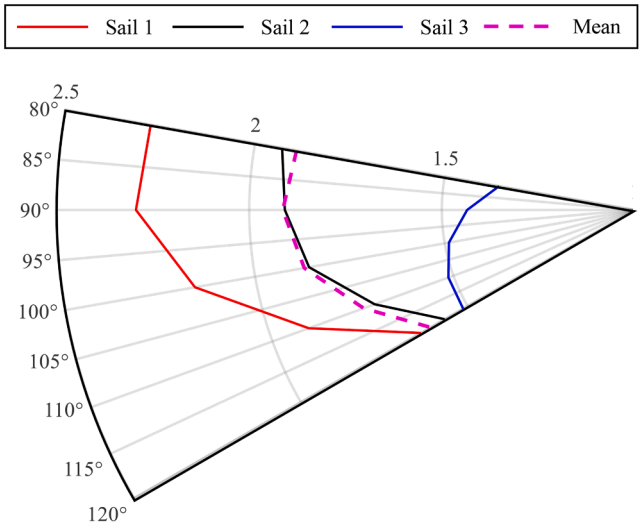


Fig. 27. Polar diagrams of C_T *vs.* θ_{AW}, based on triple-wingsail WT tests.

Table 1
Main dimensions and parameters of a typical Panamax oil tanker (full-load departure condition).

Main dimensions and parameters	Values
Length between perpendiculars (L_{PP})	240 m
Beam (B)	32 m
Draft (t)	12 m
Depth (D)	18 m
Design speed V_{S_design}	14.5 knots
Deadweight tonnage (DWT)	52,000 metric tons
Displacement (Δ)	60,000 metric tons
Total engine power (P_{total})	12,000 kW
Propeller efficiency (η)	0.62
Vertical center of gravity ($\overline{KG}$)	12 m
Metacentric height ($\overline{GM}$)	3 m

calculated using Eqs. (3) and (4). Given the total engine power (P_{total}) and propeller efficiency (η) listed in Table 1 the total thrust force from both the wingsails and the engine (F_{T_total}) is estimated to be around 1 $\times 10^6$ N using Eq. (10). This indicates that F_T and F_S generated by the wingsails are $\sim$ 23% and $\sim$ 4% of the total thrust force. Hence, the triple-wingsail system can provide an appreciable thrust, and leeway due to F_S can essentially be neglected in practice.

$$F_{T_total} = \frac{P_{total} \cdot \eta}{V_{S_design}} \tag{10}$$

According to Eq. (11), given that the height of the mast (H_{mast}) is 4 m [75], the heeling moment (M_H) caused by F_S can be around 2.4 $\times$ 10^6 N·m. The resulting heeling angle (θ_H) can be estimated by Eq. (12), which indicates that θ_H is around 1°. Hence, the static influence of the wingsails on the ship is relatively slight. However, as the wind force interacts with the wingsails, it can induce rolling motions. Due to the large moment arms, F_S generated by wingsails can potentially cause dynamic rolling of the ship, which is expected to be addressed in further studies.

$$M_H = F_S \cdot \left(D + \frac{H}{2} + H_{mast} \right) \tag{11}$$

$$\theta_H = \frac{M_H}{\Delta \cdot \overline{GM}} \tag{12}$$

4. Conclusion

This study presents experimental and numerical investigations for a cambered thick wingsail, which is operated at high *Re* in practice. The analysis of the model-scale aerodynamic performance encompasses the first experimental data set for crescent airfoils in single and multiple wingsail configurations. The *Re* sensitivity of the aerodynamic performance is proven experimentally and discussed.

The model tests demonstrated that the crescent wingsail generates significant thrust under various angles of attack (α). The lift and drag coefficients with respect to α provide the first experimental data supporting the validity of previous numerical studies. At sufficiently high *Re*, high lift is achieved over a wide range of α (from around 10° to 35°). By analyzing the curves of the lift and drag coefficients as a function of α at different *Re*, a sudden drop in lift and an increase in drag are observed at α of 15°, when *Re* is reduced from 3.1 $\times 10^5$ to 2.7 $\times 10^5$. A similar crisis of the aerodynamic forces was also reported for other blunt bodies, such as circular cylinders. The aerodynamic forces are sensitive to *Re* within the tested range, since the laminar-turbulent transition and flow separation are changed.

In the triple-sail arrangement, notable interferences between the wingsails are observed. The effect is dependent on the apparent wind angle. The load distribution between the wingsails is non-uniform, with

the largest propulsion generated by the upstream (bow) wingsail and the smallest propulsion by the downstream (stern) wingsail. However, the mean F_T generated by the three wingsails is close to that of an isolated single wingsail, so the non-uniformly distributed loads do not affect the overall performance of the system.

Unlike our earlier numerical studies, this work provides the first experimental dataset for crescent-shaped thick wingsails at moderate Reynolds numbers. It also establishes, for the first time, a consistent link between model-scale and full-scale aerodynamic mechanisms, highlighting critical differences such as the occurrence of force crises at model scale but not at full scale. Furthermore, the present study uniquely reveals the interference mechanisms in a triple-wingsail configuration, offering new physical insights that have not been addressed in previous publications.

The vertical wind profiles, *i.e.*, the wind gradient, are neglected in this study. When predicting the propulsive performance, the wingsails are assumed to be installed on a relatively large horizontal plate, and the interactions with the hull and superstructures are neglected. For the triple-wingsail configuration, the effects of the distance between wingsails are beyond the scope of the present study. These aspects will be interesting in future work. In addition, although the CFD results provide physically consistent flow-field information and have been cross-checked against experimental force measurements, direct flow-field validation (*e.g.*, PIV) has not been conducted in the present work. Future studies incorporating such measurements would further enhance the understanding and validation of the flow mechanisms around crescent-shaped wingsails.

Data availability

The data that support the findings of this study are available from the corresponding author, Heng Zhu, upon reasonable request.

CRediT authorship contribution statement

Heng Zhu: Conceptualization, Methodology, Validation, Formal analysis, Data Curation, Writing - Original Draft, Visualization. **Valery Chernoray**: Methodology, Investigation, Resources, Data Curation, Writing - Review & Editing. **Jonas W. Ringsberg**: Conceptualization, Resources, Writing - Review & Editing, Supervision, Project administration. **Bengt Ramne**: Conceptualization, Resources, Writing - Review & Editing, Supervision, Funding acquisition. **Hua-Dong Yao**: Conceptualization, Methodology, Resources, Writing - Review & Editing, Supervision, Project administration.

Declaration of competing interest

The authors declare that they have no known competing financial interests or personal relationships that could have appeared to influence the work reported in this paper.

Acknowledgments

This work was performed within the project “WindStruc”, co-funded by ScandiNAOS AB, the Swedish Energy Agency (no. 51552-1), and Stena Rederi AB. It also received funding from Chalmers University of Technology Foundation for the strategic research project “Hydro- and aerodynamics”, and from the Swedish Transport Administration (no. 2023/32107) for the project “GEMINI” (Generic multidisciplinary optimization for sail installation on wind-assisted ships). During the process of this study, three interns at Chalmers University of Technology: Paul Masson, Thibault Mergault, and Baptiste Morvan also offered help in wind tunnel tests. The computations and data handling were enabled by resources provided by the National Academic Infrastructure for Supercomputing in Sweden (NAISS), partially funded by the Swedish Research Council through grant agreement no. 2022-06725.

Supplementary materials

Supplementary material associated with this article can be found, in the online version, at doi:10.1016/j.joes.2026.08.012.

References

[1] UNCTAD, Review of Maritime Transport 2023, United Nations, 2023.
[2] IMO. (2018). Interpretation of initial IMO strategy on reduction of GHG emissions from ships. In (Vol. 60, pp. 195–201).
[3] L. Khan, J. Macklin, B. Peck, O. Morton, J.-B.R.G. Souppez, A review of wind-assisted ship propulsion for sustainable commercial shipping: latest developments and future stakes, in: Proceedings of the Wind Propulsion Conference 2021, London, UK, 2021.
[4] F. Thies, K. Fakiolas, Wind propulsion. Sustainable Energy Systems On Ships, Elsevier, 2022, pp. 353–402.
[5] H. Zhu, Methods for the Evaluation of Wingsails with a Crescent-Shaped Profile, Licentiate thesis, Chalmers University of Technology, Gothenburg, Sweden, 2023.
[6] D.W. Atkins, The CFD Assisted Design and Experimental Testing of a Wing-Sail with High Lift Devices, PhD thesis, University of Salford, Salford, UK, 1996.
[7] G. Atkinson, H. Nguyen, J. Binns, Considerations regarding the use of rigid sails on modern powered ships, Cogent Eng. 5 (1) (2018) 1543564, https://doi.org/10.1080/23311916.2018.1543564.
[8] K. Ouchi, K. Uzawa, A. Kanai, Huge hard wing sails for the propulsor of next generation sailing vessel, in: Second International Symposium on Marine Propulsors, Hamburg, Germany, 2011.
[9] Chen, Z., Cai, W., & Zeng, Q. (2022). A numerical study on the thrust and interaction of a three-sail wind-assisted propulsion system. Proceedings of the ASME 2022, 41st International Conference on Ocean, Offshore and Arctic.
[10] M. Nikmanesh, Sailing Performance Analysis Using CFD Simulations: A Study on Crescent Shaped Wing Profiles, Master's thesis, Chalmers University of Technology, Gothenburg, Sweden, 2021.
[11] H. Zhu, V. Chernoray, H.-D. Yao, J.W. Ringsberg, B. Ramne, Experimental study on structure responses of triple wing sails to turbulence flows at multiple apparent wind angles, in: 9th International Conference on Marine Structures, MarStruct, Gothenburg, Sweden, 2023.
[12] H. Zhu, V. Chernoray, H.-D. Yao, J.W. Ringsberg, B. Ramne, Fluid-structure interaction analysis of crescent-shaped wingsails, in: Proceedings of the International Conference on Offshore Mechanics and Arctic Engineering - OMAE, Singapore, Singapore, 2024.
[13] A. Blakeley, R. Flay, P. Richards, Design and optimisation of multi-element wing sails for multihull yachts. 18th Australasian Fluid Mechanics Conference, Launceston, Australia, 2012.
[14] C. Li, H. Wang, P. Sun, Numerical investigation of a two-element wingsail for ship auxiliary propulsion, J. Mar. Sci. Eng. 8 (5) (2020) 333, https://doi.org/10.3390/jmse8050333.
[15] A.M.O. Smith, High-lift aerodynamics, J. Aircr. 12 (6) (1975) 501–530.
[16] L. Kuang, H. Li, X. Su, X. Song, Z. Wang, Y. Zhang, W. Ma, Effect of chord length ratio on aerodynamic performance of two-element wing sail, Ocean Eng. 287 (2023) 115946.
[17] D. Li, Y. Zhang, P. Li, J. Dai, G. Li, Aerodynamic performance of a new double-flap wing sail, Pol. Marit. Res. 26 (4) (2019) 61–68.
[18] G.M. Atkinson, Analysis of lift, drag and CX polar graph for a 3D segment rigid sail using CFD analysis, J. Mar. Eng. Technol. 18 (1) (2019) 36–45, https://doi.org/10.1080/20464177.2018.1494953.
[19] G.M. Atkinson, J. Binns, Power profile for segment rigid sail, J. Mar. Eng. Technol. 17 (2) (2018) 99–105, https://doi.org/10.1080/20464177.2017.1319997.
[20] K. Ouchi, K. Uzawa, A. Kanai, M. Katori, Wind challenge" the next generation hybrid sailing vessel. The Third International Symposium on Marine Propulsors, Launceston, Tasmania, Australia, Launceston, Tasmania, Australia, 2013.
[21] I.M. Viola, M. Sacher, J. Xu, F. Wang, A numerical method for the design of ships with wind-assisted propulsion, Ocean Eng. 105 (2015) 33–42, https://doi.org/10.1016/j.oceaneng.2015.06.009.
[22] R. Zhang, L. Huang, G. Peng, R. Ma, K. Wang, F. Tian, Q. Song, A novel method of desynchronized operation of sails for ship wind-assisted propulsion system, Ocean Eng. 288 (2023) 115964.
[23] H. Zhu, M.B. Nikmanesh, H.D. Yao, B. Ramne, J.W. Ringsberg, Propulsive performance of a novel crescent-shaped wind sail analyzed with unsteady rans, in: Proceedings of the International Conference on Offshore Mechanics and Arctic Engineering - OMAE, Hamburg, Germany, 2022.
[24] G. Bordogna, J.A. Keuning, R.H.M. Huijsmans, M. Belloli, Wind-tunnel experiments on the aerodynamic interaction between two rigid sails used for wind-assisted propulsion, Int. Shipbuild. Prog. 65 (1) (2018) 93–125.
[25] Burden, A., Lloyd, T., Mockler, S., Mortola, L., Shin, I.B., & Smith, B. (2010). Concept design of a fast sail assisted feeder container ship.
[26] H. Furukawa, A.W. Blakeley, R.G.J. Flay, P.J. Richards, Performance of wing sail with multi element by two-dimensional wind tunnel investigations, J. Fluid Sci. Technol. 10 (2) (2015) JFST0019. -JFST0019.
[27] L.M. Giovannetti, U. Dhome, K. Malmek, A. Persson, C. Wielgosz, Multi-wing sails interaction effects, in: SNAME Chesapeake Sailing Yacht Symposium, 2022.
[28] N. Aubin, B. Augier, J. Deparday, M. Sacher, P. Bot, Performance enhancement of downwind sails due to leading edge flapping: a wind tunnel investigation, Ocean Eng. 169 (2018) 370–378.

[29] J.-B.R. Souppez, I.M. Viola, Water tunnel testing of downwind yacht sails, Exp. Fluids 65 (2) (2024) 1–19.
[30] I.M. Viola, Recent advances in sailing yacht aerodynamics, Appl. Mech. Rev. 65 (4) (2013) 040801.
[31] I.M. Viola, R.G. Flay, Sail pressures from full-scale, wind-tunnel and numerical investigations, Ocean Eng. 38 (16) (2011) 1733–1743.
[32] I.M. Viola, R.G. Flay, Sail aerodynamics: on-water pressure measurements on a downwind sail, J. Ship Res. 56 (04) (2012) 197–206.
[33] L. Larsson, Scientific methods in yacht design, Annu. Rev. Fluid Mech. 22 (1) (1990) 349–385.
[34] K. Malmek, L. Larsson, S. Werner, J.W. Ringsberg, R. Bensow, C. Finnsgård, Rapid aerodynamic method for predicting the performance of interacting wing sails, Ocean Eng. 293 (2024) 116596, https://doi.org/10.1016/j.oceaneng.2023.116596.
[35] H. Zhu, H.-D. Yao, F. Thies, J.W. Ringsberg, B. Ramne, Propulsive performance of a rigid wingsail with crescent-shaped profiles, Ocean Eng. 285 (2023) 115349, https://doi.org/10.1016/j.oceaneng.2023.115349.
[36] J. Kimball, Physics of Sailing, CRC Press, 2009, https://doi.org/10.1201/9781420073775.
[37] W. Püschl, High-speed sailing, Eur. J. Phys. 39 (4) (2018) 044002.
[38] D. Li, G. Li, J. Dai, P. Li, A new type of collapsible wing sail and its aerodynamic performance, Int. Conf. Offshore Mech. Arct. Eng. (2017).
[39] H. Blount, J.M. Portell, CFD Investigation of Wind Powered Ships Under Extreme Conditions Gothenburg, 2021.
[40] H. Zhu, CFD Investigation of Wind-Powered Ships under Extreme Condition: Simulations on the NACA-0015 Foil under Deep Stall Condition, Master's thesis, Chalmers University of Technology, Gothenburg, Sweden, 2020.
[41] P. Fagerlund, B. Ramne, Teleskopiskt Segelarrangemang, 2010.
[42] A. Borgoltz, N. Intaratep, W.J. Devenport, Aerodynamic Effects of Boundary Layer Trip Strips On the Flow over a NACA63018 Airfoil, Virginia Polytechnic Inst. and State Univ., Blacksburg, VA, 2019.
[43] A. Rona, H. Soueid, Boundary layer trips for low Reynolds number wind tunnel tests, in: 48th AIAA Aerospace Sciences Meeting Including the New Horizons Forum and Aerospace Exposition, 2010.
[44] N.T. Hoang, B.V. Bui, Investigation of wind tunnel wall effect and wing-fuselage interference regarding the prediction of wing aerodynamics and its influence on the horizontal tail, J. Mech. Sci. Technol. 33 (2019) 2737–2746.
[45] K. Xu, X. Su, I. Jonsson, R. Bensow, S. Krajnovic, Numerical study of a generic ship's airwake for understanding bi-stability mechanism, J. Fluid Mech. 991 (2024) A6.
[46] H. Schlichting, K. Gersten, Boundary-layer Theory, springer, 2016.
[47] J.B. Barlow, W.H. Rae, A. Pope. Low-Speed Wind Tunnel Testing, John Wiley & Sons, 1999.
[48] F. Russo, N.T. Basse, Scaling of turbulence intensity for low-speed flow in smooth pipes, Flow Meas. Instrum. 52 (2016) 101–114.
[49] M.L. Shur, P.R. Spalart, M.K. Strelets, A.K. Travin, A hybrid RANS-LES approach with delayed-DES and wall-modelled LES capabilities, Int. J. Heat Fluid Flow 29 (6) (2008) 1638–1649, https://doi.org/10.1016/j.ijheatfluidflow.2008.07.001.
[50] L. Davidson, Fluid mechanics, turbulent flow and turbulence modeling. Division of Fluid Dynamics, Department of Mechanics and Maritime Sciences Chalmers University of Technology, 2019.
[51] F.R. Menter, Zonal two equation κ-ω turbulence models for aerodynamic flows, in: AIAA 23rd Fluid Dynamics, Plasmadynamics, and Lasers Conference, Orlando,FL, U.S.A, 1993.
[52] Wilcox, D.C. (1989). Turbulence modeling for CFD (Vol. 27).
[53] H. Reichardt, Vollständige darstellung der turbulenten geschwindigkeitsverteilung in glatten Leitungen, ZAMM - J. Appl. Math. Mech. /Z. Angew. Math. Mech. 31 (7) (1951) 208–219, https://doi.org/10.1002/ZAMM.19510310704.
[54] T. Barth, D. Jespersen, The design and application of upwind schemes on unstructured meshes, 27th Aerosp. Sci. Meet. (1989).
[55] B.P. Leonard, Simple high-accuracy resolution program for convective modelling of discontinuities, Int. J. Numer. Methods Fluids 8 (10) (1988) 1291–1318.
[56] S.V. Patankar, Numerical Heat Transfer and Fluid Flow, CRC Press, 1981, https://doi.org/10.13182/nse81-a20112.
[57] Siemens PLM Software, STAR-CCM+ User Guide (version 16.02), Siemens PLM Software Inc, Munich, Germany, 2021.
[58] J.-B.R. Souppez, P. Bot, I.M. Viola, Turbulent flow around circular arcs, Phys. Fluids 34 (1) (2022).
[59] F.W. Schmitz, Research and …, Redstone Scientific Information Center, 1970. Translation Branch.
[60] J. Tank, B. Klose, G. Jacobs, G. Spedding, Flow transitions on a cambered airfoil at moderate Reynolds number, Phys. Fluids 33 (9) (2021).
[61] D.S. Holloway, D.K. Walters, J.H. Leylek, Prediction of unsteady, separated boundary layer over a blunt body for laminar, turbulent, and transitional flow, Int. J. Numer. Methods Fluids 45 (12) (2004) 1291–1315.
[62] J. Hoffman, C. Johnson, Laminar and turbulent flow, Comput. Turbul. Incompressible Flow: Appl. Math.: Body Soul 4 (2007) 51–55.
[63] P. Bot, Force variations related to flow pattern changes around a high-camber thin wing, AIAA J. 58 (5) (2020) 1906–1912.
[64] P. Bot, M. Rabaud, G. Thomas, A. Lombardi, C. Lebret, Sharp transition in the lift force of a fluid flowing past nonsymmetrical obstacles: evidence for a lift crisis in the drag crisis regime, Phys. Rev. Lett. 117 (23) (2016) 234501.
[65] J.-B.R.G. Souppez, Water Tunnel Testing of Highly-Cambered Plates and Wings for Downwind Yacht Sail Applications, PhD thesis, University of Edinburgh, Edinburgh, UK, 2024, https://doi.org/10.7488/era/4235.
[66] Q. Zeng, X. Zhang, W. Cai, Y. Zhou, Wake distortion analysis of a Dynarig and its application in a sail array design, Ocean Eng. 278 (2023) 114341, https://doi.org/10.1016/j.oceaneng.2023.114341.
[67] H. Zhu, Analysis and Evaluation of Wingsails with Crescent-Shaped Profiles: From Aerodynamics to Aeroelasticity, PhD thesis, Chalmers University of Technology, Gothenburg, Sweden, 2024.
[68] Marsden, D., Simpson, R., & Rainbird, W. (1957). The flow over delta wings at low speeds with leading edge separation.
[69] Henderson, A.D., & Walker, G.J. (2010). Observations of transition phenomena on a controlled diffusion compressor stator with a circular arc leading edge.
[70] J. Robert, B. Newman, Lift and drag of a sail aerofoil, Wind Eng. (1979) 1–22.
[71] J. Hou, K.P. Mok, S. Cantos, C. Bertin, K.Y. Chan, P. Zhou, S. Zhong, X. Zhang, Numerical simulation of windsurfing sail aerodynamics: insights into forces and flow characteristics, Ocean Eng. 300 (2024) 117477.
[72] A. Persson, D.Q. Li, F. Olsson, S. Werner, U. Dhomé, Performance prediction of wind propulsion systems using 3D CFD and route simulation, in: RINA, Royal Institution of Naval Architects-International Conference on Wind Propulsion, London, United Kingdom, 2019. WP 2019, 15-16 October 2019.
[73] I.M. Viola, R.G. Flay, Sail aerodynamics: understanding pressure distributions on upwind sails, Exp. Therm. Fluid Sci. 35 (8) (2011) 1497–1504.
[74] T. Cunliffe, The Complete Day Skipper: Skippering with Confidence Right From the Start, Bloomsbury Publishing, 2016, 5th ed.
[75] H. Zhu, H.-D. Yao, J.W. Ringsberg, Unsteady RANS and IDDES studies on a telescopic crescent-shaped wingsail, Sh. Offshore Struct. 19 (2024) 134–147, https://doi.org/10.1080/17445302.2023.2256601.